Multiphysics of Multilayered and Functionally Graded Cylinders Under Prescribed Hygrothermomagnetoelectro-mechanical Loading

A. H. Akbarzadeh
Post-Doctoral Fellow
e-mail: hamid.akbarzadeh@mcgill.ca

D. Pasini[1]
Associate Professor
e-mail: damiano.pasini@mcgill.ca

Department of Mechanical Engineering,
McGill University,
Montreal, QC H3A 0C3, Canada

This paper examines the multiphysics of multilayered and functionally graded cylinders subjected to steady-state hygrothermomagnetoelectromechanical loading. The cylinder is assumed to be axisymmetric, infinitely long, and with either hollow or solid cross section that is, both polarized and magnetized radially. The multiphysics model is used to investigate the effect of moisture, temperature, magnetic, electric, and mechanical loadings. The influence of imperfectly bonded interfaces is also accounted for in the governing equations. Exact solutions of differential equations are obtained for each homogenous layer of the multilayered cylinder. The results are verified with those available in literature for a homogenous infinitely long cylinder and can also be applied to study the multiphysics of thin circular disks. Maps are presented for solid and hollow cylinders to visualize the effect of hygrothermomagnetoelectromechanical loading, heterogeneity of bonded layers, and imperfectly bonded interfaces. The plots offer insight into the behavior of heterogeneous magnetoelectroelastic media in a steady state hygrothermal field.
[DOI: 10.1115/1.4025529]

Keywords: functionally graded material, hygrothermomagnetoelectroelasticity, imperfectly bonded interface, infinitely long cylinder, multilayered smart composite, multiphysics, thin circular disk

1 Introduction

Multiphysics is defined as the simulation of interactions among physical fields acting simultaneously. It is typically described by a set of partial differential equations, which are often strongly coupled [1]. As stated by Brown and Messina [2], the coupled models can often span multiple length scales, an additional complexity that makes multiphysics problems challenging. The coupled interaction of physical phenomena may involve elastic, electric, magnetic, thermal, hygroscopic, chemical, and optical fields. This scenario might be observed in natural (wood, bone, and liquid crystals) or synthetic (piezoelectric, piezomagnetic, magnetoelectroelastic (MEE), and polyelectrolyte gels) smart materials [3]. Multiphysics analysis is a critical step to several applications involving structural health monitoring, intelligent structures, energy harvesting and green energy production, optics, space vehicles, and self-powered biomedical devices [4]. While the coupling of four physical fields has been investigated for laminated hygrothermopiezoelectric plates [4], only recently the concurrent influence of multiple fields, such as moisture, temperature, magnetic, electric, and mechanical, has been object of investigation [5].

In recent years, several studies have implemented microscopic and macroscopic multiphysics analysis. Huang and Kuo [6] obtained the MEE tensor analogous to the Eshelby tensor for elastic ellipsoidal inclusions. Later, Li and Dunn [7] employed the micromechanics Mori–Tanaka mean field approach to obtain the effective moduli of heterogeneous MEE multiphysics media. Thermally induced vibration of hygrothermopiezoelectric laminated plates and shells was analyzed by Raja et al. [8]. Georgiades et al. [9] applied the three-dimensional (3D) micromechanical model based on the asymptotic homogenization of thin smart plates reinforced by piezoelectric bars. Subsequently, Hassan et al. [10] obtained a micromechanical model for smart 3D composites reinforced by a periodic piezoelectric grid. The behavior of parallel permeable cracks in an MEE medium subjected to antiplane shear loading was investigated by Zhang et al. [11]. Kundu and Han [12] studied the hygrothermoelastic buckling responses of laminated shells using the nonlinear finite element method (FEM). Chen [13] developed a theory of nonlinear thermoelectroviscoelasticity with inclusion of hysteresis, aging, and damage effects. Mahato and Maiti [14] used active fiber composites to control undesirable responses caused by hygrothermal conditions. Babaei and Akhras [15] obtained a closed-form solution for the behavior of a radially polarized piezoelectric cylinder working at different temperature. To compare the coupled multiphysics theories, Akbarzadeh et al. [16] studied the thermopiezoelectricity in a functionally graded piezoelectric (FGP) medium. The influence of hygrothermal effects on free vibration of laminated plates with temperature- and moisture-dependent material properties was investigated by Kumar et al. [17]. An efficient beam model was developed by Wang and Yu [18] to study the multiphysics behavior of MEE structures using the variational asymptotic method. A closed-form solution was obtained by Akbarzadeh et al. [19] for classical coupled thermoelasticity in functionally graded (FG) rectangular. Faruque Ali and Adhikari [20] analyzed the application of a vibration absorber supplemented with a piezoelectric stack for energy harvesting. Recently, Kondaiah et al. [21] studied pyroelectric and pyromagnetic effects on multiphysics responses of MEE cylindrical shells.

Multiphysics simulation of multilayered composites with perfectly/imperfectly bonded interfaces is of great significance for

[1]Corresponding author.
Manuscript received July 17, 2013; final manuscript received September 16, 2013; accepted manuscript posted September 25, 2013; published online November 13, 2013. Assoc. Editor: Glaucio H. Paulino.

applications where there is a need to inhibit debonding, crack initiation, and fracture as the discontinuity of material properties across interfaces and bonding imperfections play an important role in the structural response. Multilayered smart composites with stacked layers of integrated piezoelectric/piezomagnetic fibers or bonded piezoelectric/piezomagnetic layers to base matrices are being used for their low density and superior mechanical and hygrothermal properties as well as sensing and actuation [22,23].

Multiphysics responses of smart composites have attracted the interest of several researchers. For instance, Xu et al. [24] presented a closed-form solution for coupled thermoelectroelastic responses of multilayered plates. Pan [25] derived exact solutions for anisotropic, simply supported, MEE multilayered plates. A general stress analysis for multilayered cylinders under hygrothermal loadings was developed by Sayman [26]. Shi et al. [27] studied multilayered piezoelectric beams based on the linear electroelasticity theory. Balamurugan and Narayanan [28] presented a piezolaminated element for finite element analysis of multilayered plates. A simply supported MEE cylinder was investigated by Daga et al. [29] using Fourier series expansion and FEM. Wang et al. [30] studied the dynamic behavior of a perfectly bonded multilayered smart composite using a hybrid method. The effective matrices of a multilayered beam with FG layers were derived by Murin and Kutis [31] using FEM. Wang et al. [32] obtained closed-form solutions for a transversely isotropic multilayered MEE circular plate. A multilayered piezoelectric/piezomagnetic composite with periodic interface cracks was studied by Wan et al. [33]. A new finite element model was presented by Milazzo and Orlando [34] based on an equivalent single-layer model for MEE multilayered structures. Brischetto [35] proposed a refined two-dimensional (2D) model for the hygrothermoelastic analysis of doubly curved sandwich shells.

The interface between two bodies is imperfect in the presence of discontinuities when, for example, microstructural defects such as voids and cracks exist on the boundaries [36]. To model dilute composites with circular inclusions and imperfectly bonded interfaces, Bigoni et al. [37] applied an asymptotic scheme. Icardi [38] investigated the static, free vibration, and buckling of laminated plates with bonding imperfections. Chen et al. [39] explored the bending and free vibration of an imperfectly bonded piezoelectric rectangular laminate using the state-space approach. Adrianov et al. [40] proposed an asymptotic approach to simulate imperfect bonding in composite materials. Later on, Mitra and Gopalakrishnan [41] studied the wave propagation in a single-walled carbon nanotube with discontinuous connection. The MEE responses of multiferroic composites with imperfect interface were also studied by Wang and Pan [42]. Melkumyan and Mai [43] investigated interface waves caused by imperfectly bonded piezoelectric and piezomagnetic half-spaces. Fan and Sze [36] proposed a micromechanics model based on the self-consistent scheme for imperfect dielectric bodies. Finally, Wang and Zou [44] developed a model to analyze a piezoelectric cantilevered energy harvester with imperfectly bonded interfaces.

FG smart materials with continuous transition of material properties throughout the domain have been proposed to avoid failure and discontinuity of multiphysics fields in conventional laminated smart composites. FG structures also benefit from their multiphysics properties on the surfaces that enhance their compatibility for various applications [45,46]. Accordingly, investigation on multiphysics analysis of FG intelligent structures is essential for promoting their applications.

Since the emergence of functionally graded materials (FGMs), abundant papers studying their structural behavior have been published. Pan and Han [47] presented an exact solution for FG MEE plates using the Stroh-type solution formalism. Zhou et al. [48] studied the behavior of a crack in an FG MEE medium. Wang and Ding [49] obtained a closed-form solution to investigate the transient response of FG MEE hollow cylinders. The fracture of FGP materials with a dielectric crack model was investigated by Jiang [50]. Shen [51] studied the nonlinear bending of FG nanocomposite plates reinforced by carbon nanotubes. A closed-form solution for bonded FG MEE half-planes was derived by Lee and Ma [52]. Akbarzadeh et al. [53] investigated the thermal induced vibration of an FG plate via the hybrid Laplace–Fourier transform. The static, dynamic, and free vibration analysis of doubly curved FG panels resting on Pasternak-type elastic foundation was studied by Kiani et al. [54]. Panda and Sopan [55] solved finite element equations for nonlinear analysis of thermoelectroelastic FG sector plates. More recently, Kiani et al. [56] presented a scheme for active control of doubly curved FG panels.

The hygrothermopiezoelectric model was introduced by Smittakorn and Heyliger [57]; later, Akbarzadeh and Chen [5] developed a hygrothermomagnetoelectroelastic model and applied for the analysis of a homogenous cylinder. Yet, the multiphysics analysis of multilayered or functionally graded smart cylinders rested on an elastic foundation with plane strain/plane stress condition has not been considered. This paper examines the steady-state hygrothermomagnetoelectroelastic response of multilayered and FG cylinders with plane strain/plane stress conditions. The composite cylinders are assumed to be axisymmetric, radially polarized, and radially magnetized, in the presence of a hygrothermal field. The governing differential equations are first decoupled and then solved in an exact form by imposing perfect/imperfect interfacial conditions as well as boundary conditions. Finally, the influence of multiphysics loading, bonding imperfections, heterogeneity, and nonhomogeneity indices are visualized in maps that help to gain insight into multiphysics responses of the heterogeneous cylinders.

2 Problem Definition and Governing Equations

This section presents the governing equations, including constitutive, potential field, and conservation equations, for steady-state hygrothermomagnetoelectroelastic responses of an axisymmetric cylinder with multilayered or FG cross section (Fig. 1).

We assume a multilayered hollow MEE cylinder with plane strain or plane stress condition subjected to a combined disturbance of hygroscopic, thermal, magnetic, electric, and mechanical loading. The MEE cylinder experiences on its inner and outer surfaces changes in moisture concentration m, temperature ϑ, magnetic potential φ, electric potential ϕ, and pressure P (Fig. 1). We consider also that these loadings are applied solely on the outer surface.

To derive the governing equations and boundary conditions in a general format, we consider the MEE cylinder as rotating with angular velocity ω, about the z-axis in a cylindrical coordinate system (r, θ, z), and resting on a Winkler-type elastic foundation with foundation stiffness k_w. The number of layers is represented by N; $R_n (n = 1, 2, \ldots, N)$ is the outer radius of the n-th layer and $R_0 = a$ is the inner radius for the first layer and $R_n = b$ is the outer radius of N-th layer of the hollow multilayered MEE cylinder. For a solid multilayered MEE cylinder constructed of an solid core and N-1 hollow cylindrical layers, $R_0 = 0$.

In linear hygrothermomagnetoelectroelasticity, the constitutive equations for each layer of a multilayered composite can be written as [5,58]

$$\begin{aligned}
\sigma_{ij}^{(n)} &= C_{ijkl}^{(n)}\varepsilon_{kl}^{(n)} - e_{kij}^{(n)}E_k^{(n)} - d_{kij}^{(n)}H_k^{(n)} - \beta_{ij}^{(n)}\vartheta^{(n)} - \xi_{ij}^{(n)}m^{(n)} \\
D_i^{(n)} &= e_{ijk}^{(n)}\varepsilon_{jk}^{(n)} + \in_{ij}^{(n)} E_j^{(n)} + g_{ij}^{(n)}H_j^{(n)} + \gamma_i^{(n)}\vartheta^{(n)} + \chi_i^{(n)}m^{(n)} \\
B_i^{(n)} &= d_{ijk}^{(n)}\varepsilon_{jk}^{(n)} + g_{ij}^{(n)}E_j^{(n)} + \mu_{ij}^{(n)}H_j^{(n)} + \tau_i^{(n)}\vartheta^{(n)} + \upsilon_i^{(n)}m^{(n)} \\
&\quad \times (n = 1, 2, \ldots, N)
\end{aligned} \tag{1}$$

where $\sigma_{ij}^{(n)}$, $D_i^{(n)}$, $B_i^{(n)}$, $\varepsilon_{ij}^{(n)}$, $E_i^{(n)}$, $H_i^{(n)}$, $\vartheta^{(n)}$, and $m^{(n)}$ $(n = 1, 2, \ldots, N\ i, j, k, l = 1, 2, 3)$ are stress tensor, electric displacement vector, magnetic induction vector, strain tensor, electric field vector, magnetic field vector, temperature change, and

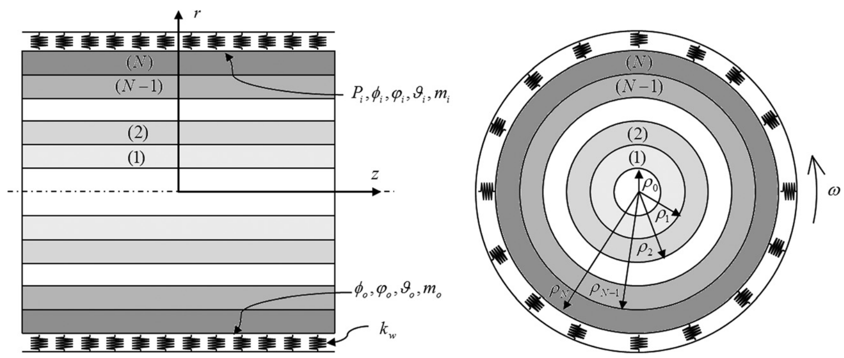

Fig. 1 Rotating hollow multilayered MEE cylinder resting on elastic foundation and its multiphysics boundary conditions; subscripts "i" and "o" indicate inner and outer surfaces

moisture concentration change, respectively; $C_{ijkl}^{(n)}$, $e_{ijk}^{(n)}$, $d_{ijk}^{(n)}$, $\in_{ij}^{(n)}$, $g_{ij}^{(n)}$, $\mu_{ij}^{(n)}$, $\beta_{ij}^{(n)}$, $\xi_{ij}^{(n)}$, $\gamma_i^{(n)}$, $\chi_i^{(n)}$, $\tau_i^{(n)}$, and $\upsilon_i^{(n)}$ are, respectively, elastic, piezoelectric, piezomagnetic, dielectric, electromagnetic, magnetic permeability, thermal stress, and hygroscopic stress coefficient tensors and pyroelectric, hygroelectric, pyromagnetic, and hygromagnetic coefficients vectors. In addition, $\vartheta^{(n)} = T^{(n)} - T_0$ and $m^{(n)} = C^{(n)} - C_0$ where in, T and C represent the absolute temperature and moisture concentration, and T_0 and C_0 are the stress-free temperature and moisture concentration, respectively. The thermal stress and hygroscopic stress coefficient tensors are also related to the elastic coefficient tensor $C_{ijkl}^{(n)}$, the thermal expansion coefficient tensor $\alpha_{ij}^{T(n)}$, and the moisture expansion coefficient tensor $\beta_{ij}^{C(n)}$ by $\beta_{ij}^{(n)} = C_{ijkl}^{(n)}\alpha_{kl}^{T(n)}$ and $\xi_{ij}^{(n)} = C_{ijkl}^{(n)}\beta_{kl}^{C(n)}$.

The linear potential field equations, including strain-displacement and quasi-stationary electromagnetic field equations, are specified as [59]

$$\varepsilon_{ij}^{(n)} = \frac{1}{2}\left(u_{i,j}^{(n)} + u_{j,i}^{(n)}\right); \quad E_i^{(n)} = -\phi_{,i}^{(n)}; \quad H_i^{(n)} = -\varphi_{,i}^{(n)} \tag{2}$$

in which $u_i^{(n)}$, $\phi^{(n)}$, and $\varphi^{(n)}$ stand, respectively, for displacement vector, electric potential, and magnetic potential; the comma represents the differentiation operator. Furthermore, in the absence of body force, free charge density, and current density, the equations of motion and Maxwell's electromagnetic field are written as [60]

$$\sigma_{ij,j}^{(n)} = \rho_d^{(n)} u_{i,tt}^{(n)}; \quad D_{i,i}^{(n)} = 0; \quad B_{i,i}^{(n)} = 0 \tag{3}$$

where $\rho_d^{(n)}$ stands for mass density and t represents time. The governing equations (1)–(3) could be further simplified for axisymmetric plane strain and plane stress conditions. The constitutive equations (1) for axisymmetric, transversely isotropic, radially polarized, and radially magnetized materials with plane strain condition (infinitely long cylinder) are written as [5]

$$\begin{aligned}
\sigma_{rr}^{(n)} &= c_{33}^{(n)} u_{,r}^{(n)} + c_{13}^{(n)} \frac{u^{(n)}}{r} + e_{33}^{(n)} \phi_{,r}^{(n)} + d_{33,r}^{(n)} \varphi_{,r} - \beta_1^{(n)} \vartheta^{(n)} - \xi_1^{(n)} m^{(n)} \\
\sigma_{\theta\theta}^{(n)} &= c_{13}^{(n)} u_{,r}^{(n)} + c_{11}^{(n)} \frac{u^{(n)}}{r} + e_{31}^{(n)} \phi_{,r}^{(n)} + d_{31}^{(n)} \varphi_{,r}^{(n)} - \beta_3^{(n)} \vartheta^{(n)} - \xi_3^{(n)} m^{(n)} \\
\sigma_{zz}^{(n)} &= c_{13}^{(n)} u_{,r}^{(n)} + c_{12}^{(n)} \frac{u^{(n)}}{r} + e_{31}^{(n)} \phi_{,r}^{(n)} + d_{31}^{(n)} \varphi_{,r}^{(n)} - \beta_3^{(n)} \vartheta^{(n)} - \xi_3^{(n)} m^{(n)} \\
D_r^{(n)} &= e_{33}^{(n)} u_{,r}^{(n)} + e_{31}^{(n)} \frac{u^{(n)}}{r} - \in_{33}^{(n)} \phi_{,r}^{(n)} - g_{33}^{(n)} \varphi_{,r}^{(n)} + \gamma_1^{(n)} \vartheta^{(n)} + \chi_1^{(n)} m^{(n)} \\
B_r^{(n)} &= d_{33}^{(n)} u_{,r}^{(n)} + d_{31}^{(n)} \frac{u^{(n)}}{r} - g_{33}^{(n)} \phi_{,r}^{(n)} - \mu_{33}^{(n)} \varphi_{,r}^{(n)} + \tau_1^{(n)} \vartheta^{(n)} + \upsilon_1^{(n)} m^{(n)}
\end{aligned} \tag{4}$$

where $u = u_r$ is the radial displacement and $c_{pq}^{(n)} = C_{ijkl}^{(n)}$, $e_{pq}^{(n)} = e_{ijkl}^{(n)}$, $d_{pq}^{(n)} = d_{ijk}^{(n)}$, $\beta_p^{(n)} = \beta_{ij}^{(n)}$ and $\xi_p^{(n)} = \xi_{ij}^{(n)}$ $(i,j,k,l = 1,2,3;\ p,q = 1,2,\ldots,6)$. The equation of motion and Maxwell's electromagnetic equations can also be rewritten as [61]

$$\begin{gathered}
\sigma_{rr,r}^{(n)} + \frac{1}{r}\left(\sigma_{rr}^{(n)} - \sigma_{\theta\theta}^{(n)}\right) = \rho_d^{(n)} u_{,tt}^{(n)}; \quad D_{r,r}^{(n)} + \frac{1}{r} D_r^{(n)} = 0 \\
B_{r,r}^{(n)} + \frac{1}{r} B_r^{(n)} = 0
\end{gathered} \tag{5}$$

It is worth noting that for rotary cylinders with angular velocity ω about the z-axis, we have: $u_{,tt} = -r\omega^2$. For plane stress condition (thin circular disk), the constitutive equations (4) with $\sigma_{zz}^{(n)} = 0$ should be modified; however, Eq. (5) is valid for plane stress. The analogy of hygrothermomagnetoelectroelastic coefficients for plane strain and plane stress is illustrated in Table 1. More details are given in Refs. [62] and [63].

It is worth mentioning that the procedure presented in this paper is for an axisymmetric infinitely long cylinder with plane strain condition; yet, the above formulation can be used by redefining the physical constants in Table 1 to obtain the multiphysics responses of an axisymmetric thin circular disk.

In steady-state hygrothermomagnetoelectroelastic analysis, hygrothermal fields are decoupled from the other physical fields. Therefore, temperature and moisture concentration distributions are found separately using the following Fourier heat conduction and Fickian moisture diffusion equations [64]:

$$q_i^{(n)} = -k_{ij}^{T(n)} \vartheta_{,j}^{(n)}; \quad p_i^{(n)} = -k_{ij}^{M(n)} m_{,j}^{(n)} \tag{6}$$

in which $q_i^{(n)}$, $p_i^{(n)}$, $k_{ij}^{T(n)}$, and $k_{ij}^{M(n)}$ are heat flux and moisture flux vectors and thermal conductivity and moisture diffusivity tensors, respectively. These equations along with the energy conservation equation and the conservation law for the mass of moisture are used to obtain the following hygrothermal equations for axisymmetric and steady-state condition [65]:

$$\frac{1}{r}\left(rk^{T(n)} \vartheta_{,r}^{(n)}\right)_{,r} = 0 \quad \text{(Heat conduction)} \tag{7a}$$

$$\frac{1}{r}\left(rk^{M(n)} m_{,r}^{(n)}\right)_{,r} = 0 \quad \text{(Moisture diffusion)} \tag{7b}$$

where, $k^{T(n)}$ and $k^{M(n)}$ are, respectively, isotropic thermal conductivity and moisture diffusivity coefficients.

3 Solution Procedure

For perfectly and imperfectly bonded multilayered composites, we use closed-form expressions for homogenous hollow or solid

Table 1 Analogy between the hygrothermomagnetoelectro-elastic coefficients for axisymmetric plane strain and plane stress conditions

Plane strain	Plane stress	Plane strain	Plane stress
$c_{11}^{(n)}$	$c_{11}^{(n)}-\dfrac{\left(c_{12}^{(n)}\right)^2}{c_{11}^{(n)}}$	$\mu_{33}^{(n)}$	$\mu_{33}^{(n)}+\dfrac{\left(d_{31}^{(n)}\right)^2}{c_{11}^{(n)}}$
$c_{12}^{(n)}$	$c_{12}^{(n)}$	$\beta_1^{(n)}$	$\beta_1^{(n)}-\dfrac{\beta_3^{(n)}c_{13}^{(n)}}{c_{11}^{(n)}}$
$c_{13}^{(n)}$	$c_{13}^{(n)}-\dfrac{c_{12}^{(n)}c_{13}^{(n)}}{c_{11}^{(n)}}$	$\beta_3^{(n)}$	$\beta_3^{(n)}-\dfrac{\beta_3^{(n)}c_{12}^{(n)}}{c_{11}^{(n)}}$
$c_{33}^{(n)}$	$c_{33}^{(n)}-\dfrac{\left(c_{13}^{(n)}\right)^2}{c_{11}^{(n)}}$	$\gamma_1^{(n)}$	$\gamma_1^{(n)}+\dfrac{\beta_3^{(n)}e_{31}^{(n)}}{c_{11}^{(n)}}$
$e_{31}^{(n)}$	$e_{31}^{(n)}-\dfrac{e_{31}^{(n)}c_{12}^{(n)}}{c_{11}^{(n)}}$	$\tau_1^{(n)}$	$\tau_1^{(n)}+\dfrac{\beta_3^{(n)}d_{31}^{(n)}}{c_{11}^{(n)}}$
$e_{33}^{(n)}$	$e_{33}^{(n)}-\dfrac{e_{31}^{(n)}c_{13}^{(n)}}{c_{11}^{(n)}}$	$\xi_1^{(n)}$	$\xi_1^{(n)}-\dfrac{\xi_3^{(n)}c_{13}^{(n)}}{c_{11}^{(n)}}$
$\in_{33}^{(n)}$	$\in_{33}^{(n)}+\dfrac{\left(e_{31}^{(n)}\right)^2}{c_{11}^{(n)}}$	$\xi_3^{(n)}$	$\xi_3^{(n)}-\dfrac{\xi_3^{(n)}c_{12}^{(n)}}{c_{11}^{(n)}}$
$d_{31}^{(n)}$	$d_{31}^{(n)}-\dfrac{d_{31}^{(n)}c_{12}^{(n)}}{c_{11}^{(n)}}$	$\chi_1^{(n)}$	$\chi_1^{(n)}+\dfrac{\xi_3^{(n)}e_{31}^{(n)}}{c_{11}^{(n)}}$
$d_{33}^{(n)}$	$d_{33}^{(n)}-\dfrac{d_{31}^{(n)}c_{13}^{(n)}}{c_{11}^{(n)}}$	$\upsilon_1^{(n)}$	$\upsilon_1^{(n)}+\dfrac{\xi_3^{(n)}d_{31}^{(n)}}{c_{11}^{(n)}}$
$g_{33}^{(n)}$	$g_{33}^{(n)}+\dfrac{e_{31}^{(n)}d_{31}^{(n)}}{c_{11}^{(n)}}$	$\rho_d^{(n)}$	$\rho_d^{(n)}$

layers with appropriate hygrothermomagnetoelectroelastic interfacial boundary conditions. The resulting model might be used for design and optimization of smart composite components and could provide a benchmark to verify alternative multiphysics theories and analysis. Moreover, the results could be used to model smart composites with temperature- and moisture-dependent material properties [5,58].

3.1 Homogenous Multiphysics Layer. For each homogenous layer of the cylinder shown in Fig. 1, we use Eqs. (4) and (5) to obtain the following set of ordinary differential equations, which are coupled and second-order and coupled:

$$\begin{aligned}
&c_{33}^{(n)}r^2u_{,rr}^{(n)}+c_{33}^{(n)}ru_{,r}^{(n)}-c_{11}^{(n)}u^{(n)}+e_{33}^{(n)}r^2\phi_{,rr}^{(n)}+(e_{33}^{(n)}-e_{31}^{(n)})r\phi_{,r}^{(n)}\\
&\quad+d_{33}^{(n)}r^2\varphi_{,rr}^{(n)}+(d_{33}^{(n)}-d_{31}^{(n)})r\varphi_{,r}^{(n)}-\beta_1^{(n)}r^2\vartheta_{,r}^{(n)}\\
&\quad-(\beta_1^{(n)}-\beta_3^{(n)})r\vartheta^{(n)}-\xi_1^{(n)}r^2m_{,r}^{(n)}-(\xi_1^{(n)}-\xi_3^{(n)})rm^{(n)}\\
&\quad+\rho_d^{(n)}r^3\omega^2=0\\
&e_{33}^{(n)}r^2u_{,rr}^{(n)}+\left(e_{31}^{(n)}+e_{33}^{(n)}\right)ru_{,r}^{(n)}-\in_{33}^{(n)}r^2\phi_{,rr}^{(n)}-\in_{33}^{(n)}r\phi_{,r}^{(n)}\\
&\quad-g_{33}^{(n)}r^2\varphi_{,rr}^{(n)}-g_{33}^{(n)}r\varphi_{,r}^{(n)}+\gamma_1^{(n)}r^2\vartheta_{,r}^{(n)}+\gamma_1^{(n)}r\vartheta^{(n)}\\
&\quad+\chi_1^{(n)}r^2m_{,r}^{(n)}+\chi_1^{(n)}rm^{(n)}=0\\
&d_{33}^{(n)}r^2u_{,rr}^{(n)}+\left(d_{31}^{(n)}+d_{33}^{(n)}\right)ru_{,r}^{(n)}-g_{33}^{(n)}r^2\phi_{,rr}^{(n)}-g_{33}^{(n)}r\phi_{,r}^{(n)}\\
&\quad-\mu_{33}^{(n)}r^2\varphi_{,rr}^{(n)}-\mu_{33}^{(n)}r\varphi_{,r}^{(n)}+\tau_1^{(n)}r^2\vartheta_{,r}^{(n)}+\tau_1^{(n)}r\vartheta^{(n)}\\
&\quad+\upsilon_1^{(n)}r^2m_{,r}^{(n)}+\upsilon_1^{(n)}rm^{(n)}=0
\end{aligned}\tag{8}$$

The equations above can be decoupled to obtain exact solutions for a homogenous layer [5]. To simplify the term decoupling, we introduce the following nondimensional parameters:

$$\begin{aligned}
&\alpha^{(n)}=\frac{c_{11}^{(n)}}{c_{33}^{(n)}};\quad \delta^{(n)}=\frac{c_{13}^{(n)}}{c_{33}^{(n)}};\quad \delta^{*(n)}=\frac{c_{12}^{(n)}}{c_{33}^{(n)}};\quad \beta^{(n)}=\frac{e_{31}^{(n)}}{e_{33}^{(n)}}\\
&\nu^{(n)}=\frac{d_{31}^{(n)}}{d_{33}^{(n)}};\quad \gamma^{(n)}=\frac{\in_{33}^{(n)}c_{33}^{(n)}}{\left(e_{33}^{(n)}\right)^2};\quad \lambda^{(n)}=\frac{\mu_{33}^{(n)}c_{33}^{(n)}}{\left(d_{33}^{(n)}\right)^2}\\
&\zeta^{(n)}=\frac{g_{33}^{(n)}c_{33}^{(n)}}{d_{33}^{(n)}e_{33}^{(n)}};\quad \eta^{(n)}=\frac{\beta_3^{(n)}}{\beta_1^{(n)}};\quad \varsigma^{(n)}=\frac{\xi_3^{(n)}}{\xi_1^{(n)}};\quad X^{(n)}=\frac{\gamma_1^{(n)}c_{33}^{(n)}}{\beta_1^{(n)}e_{33}^{(n)}}\\
&Y^{(n)}=\frac{\tau_1^{(n)}c_{33}^{(n)}}{\beta_1^{(n)}d_{33}^{(n)}};\quad V^{(n)}=\frac{\chi_1^{(n)}c_{33}^{(n)}}{\xi_1^{(n)}e_{33}^{(n)}};\quad W^{(n)}=\frac{\upsilon_1^{(n)}c_{33}^{(n)}}{\xi_1^{(n)}d_{33}^{(n)}}
\end{aligned}\tag{9}$$

and nondimensional multiphysics fields:

$$\begin{aligned}
&\Sigma_{rr}^{(n)}=\frac{\sigma_{rr}^{(n)}}{c_{33}^{(n)}};\quad \Sigma_{\theta\theta}^{(n)}=\frac{\sigma_{\theta\theta}^{(n)}}{c_{33}^{(n)}};\quad \Sigma_{zz}^{(n)}=\frac{\sigma_{zz}^{(n)}}{c_{33}^{(n)}};\quad D_{r1}^{(n)}=\frac{D_r^{(n)}}{e_{33}^{(n)}}\\
&B_{r1}^{(n)}=\frac{B_r^{(n)}}{d_{33}^{(n)}}\quad \Theta^{(n)}=\frac{\beta_1^{(n)}}{c_{33}^{(n)}}\vartheta^{(n)};\quad M^{(n)}=\frac{\xi_1^{(n)}}{c_{33}^{(n)}}m^{(n)}
\end{aligned}\tag{10}$$

3.1.1 Hollow Cylinder. The solutions of Eq. (8) for a homogenous hollow cylindrical layer are obtained through Eqs. (9) and (10) in terms of nondimensional radial coordinate $\rho=r/a$ and

$$\begin{aligned}
&U^{(n)}=\frac{u^{(n)}}{a};\quad \Phi_1^{(n)}=\frac{e_{33}^{(n)}}{ac_{33}^{(n)}}\phi^{(n)}\\
&\Psi_1^{(n)}=\frac{d_{33}^{(n)}}{ac_{33}^{(n)}}\varphi^{(n)};\quad \Omega^{(n)}=\frac{\rho_d^{(n)}\omega^2a^2}{c_{33}^{(n)}}
\end{aligned}\tag{11}$$

Details of the procedure are given in Refs. [5] and [66]. The nondimensional solutions are obtained as follows:

$$\begin{aligned}
U^{(n)}=&\frac{A^{(n)}}{a}+\frac{C^{(n)}}{a}\rho^{m^{(n)}}+\frac{D^{(n)}}{a}\rho^{-m^{(n)}}+\left(\frac{K_1^{(n)}}{a}\ln(\rho)+\frac{K_2^{(n)}}{a}\right)\rho\\
&+\frac{K_3^{(n)}}{a}\rho^3\ \text{(Radial displacement)}
\end{aligned}\tag{12a}$$

$$\begin{aligned}
\Phi_1^{(n)}=&\frac{H^{(n)}}{a}+\frac{G^{(n)}}{a}\ln(\rho)+\frac{C^{(n)}}{a}l_1^{(n)}\rho^{m^{(n)}}+\frac{D^{(n)}}{a}l_2^{(n)}\rho^{-m^{(n)}}\\
&+(l_3^{(n)}\ln(\rho)+l_4^{(n)})\frac{\rho}{a}+\frac{K_3^{(n)}l_5^{(n)}}{a}\rho^3\ \text{(Electric potential)}
\end{aligned}\tag{12b}$$

$$\begin{aligned}
\Psi_1^{(n)}=&\frac{F^{(n)}}{a}+\frac{E^{(n)}}{a}\ln(\rho)+\frac{C^{(n)}}{a}c_1^{(n)}\rho^{m^{(n)}}+\frac{D^{(n)}}{a}c_2^{(n)}\rho^{-m^{(n)}}\\
&+(c_3^{(n)}\ln(\rho)+c_4^{(n)})\frac{\rho}{a}+\frac{K_3^{(n)}c_5^{(n)}}{a}\rho^3\ \text{(Magnetic potential)}
\end{aligned}\tag{12c}$$

$$\begin{aligned}
\Sigma_{rr}^{(n)}=&\frac{\rho^{-1}}{a}(\delta^{(n)}A^{(n)}+G^{(n)}+E^{(n)})+\frac{\rho^{m^{(n)}-1}}{a}(m^{(n)}(1+l_1^{(n)}+c_1^{(n)})\\
&+\delta^{(n)})C^{(n)}+\frac{\rho^{-m^{(n)}-1}}{a}(-m^{(n)}(1+l_2^{(n)}+c_2^{(n)})+\delta^{(n)})D^{(n)}\\
&+\frac{\ln(\rho)}{a}(K_1^{(n)}(1+\delta^{(n)})+l_3^{(n)}+c_3^{(n)}-a(C_1^{(n)}+C_3^{(n)}{}_3))\\
&+\frac{1}{a}(K_1^{(n)}+(1+\delta^{(n)})K_2^{(n)}+l_3^{(n)}+l_4^{(n)}+c_3^{(n)}+c_4^{(n)}\\
&-a(C_2^{(n)}+C_4^{(n)}))+\frac{\rho^2}{a}(3(1+l_5^{(n)}+c_5^{(n)})+\delta^{(n)})K_3^{(n)}\\
&\text{(Radial stress)}
\end{aligned}\tag{12d}$$

where $A^{(n)}$, $C^{(n)}$, $D^{(n)}$, $E^{(n)}$, $F^{(n)}$, $G^{(n)}$, and $H^{(n)}$ $(n=1,2,\ldots,N)$ are MEE integration constants and $C_1^{(n)}$, $C_2^{(n)}$, $C_3^{(n)}$, and $C_4^{(n)}$ are hygrothermal integration constants; the other parameters in Eq. (12) are not given because of brevity. The other stress components, electric displacement, and magnetic induction could be obtained by using Eqs. (4) and (12). The hygrothermal integration constants are achieved from the solution of hygrothermal differential equations (7). For hollow cylindrical layers, radial temperature, and moisture concentration distributions are found as

$$\Theta^{(n)} = C_1^{(n)} \ln(\rho) + C_2^{(n)} \text{ (Temperature)} \tag{13a}$$

$$M^{(n)} = C_3^{(n)} \ln(\rho) + C_4^{(n)} \text{ (Moisture concentration)} \tag{13b}$$

All the aforementioned integration constants are obtained by imposing proper boundary and interfacial conditions. In addition, to determine the integration constants, Eqs. 12(*a*)–12(*c*) can be substituted into the first equation of Eq. (8) [5]

$$\alpha^{(n)}A^{(n)} + \nu^{(n)}E^{(n)} + \beta^{(n)}G^{(n)} = 0 \tag{14}$$

3.1.2 Solid Cylindrical Core. The multiphysics solutions of Eq. (8) for a homogenous solid cylindrical core are similarly realized in terms of nondimensional radial coordinate $\rho = r/b$ $(0 \le \rho \le 1)$ and

$$U^{(1)} = \frac{u^{(1)}}{b}; \quad \Phi_1^{(1)} = \frac{e_{33}^{(1)}}{bc_{33}^{(1)}}\phi^{(1)}$$
$$\Psi_1^{(1)} = \frac{d_{33}^{(1)}}{bc_{33}^{(1)}}\varphi^{(1)}; \quad \Omega^{(1)} = \frac{\rho_d^{(1)}\omega^2 b^2}{c_{33}^{(1)}} \tag{15}$$

It is worth noting that the first layer of the hollow or solid smart multilayered cylindrical composite is made of a hollow or solid cylindrical layer, respectively. Therefore, in this paper, the superscript $n=1$ specifies the solid layer of the cylinder. The nondimensional solutions are written as [5]

$$U^{(1)} = \frac{D^{(1)}}{b}\rho^{-m^{(1)}} + \frac{K_2^{(1)}}{b}\rho + \frac{K_3^{(1)}}{b}\rho^3 \text{ (Radial displacement)} \tag{16a}$$

$$\Phi_1^{(1)} = \frac{H^{(1)}}{b} + \frac{D^{(1)}}{b}l_2^{(1)}\rho^{-m^{(1)}} + \frac{l_4^{(1)}}{b}\rho + \frac{K_3^{(1)}l_5^{(1)}}{b}\rho^3 \text{ (Electric potential)} \tag{16b}$$

$$\Psi_1^{(1)} = \frac{F^{(1)}}{b} + \frac{D^{(1)}}{b}c_2^{(1)}\rho^{-m^{(1)}} + \frac{c_4^{(1)}}{b}\rho + \frac{K_3^{(1)}c_5^{(1)}}{b}\rho^3 \text{ (Magnetic potential)} \tag{16c}$$

$$\Sigma_{rr}^{(1)} = \frac{\rho^{-m^{(1)}-1}}{b}(-m^{(1)}(1+l_2^{(1)}+c_2^{(1)})+\delta^{(1)})D^{(1)} + \frac{1}{b}((1+\delta^{(1)})K_2^{(1)} + l_4^{(1)} + c_4^{(1)} - b(C_2^{(1)}+C_4^{(1)})) + \frac{\rho^2}{b}(3(1+l_5^{(1)}+c_5^{(1)})+\delta^{(1)})K_3^{(1)} \text{ (Radial stress)} \tag{16d}$$

in which $D^{(1)}$, $F^{(1)}$, and $H^{(1)}$ are MEE integration constants and $C_2^{(1)}$ and $C_4^{(1)}$ are hygrothermal integration constants; the other parameters in Eq. (16) are those obtained for the layer of a hollow cylinder except for the following parameters:

$$C_1^{(1)} = C_3^{(1)} = 0, \quad K_1^{(1)} = 0,$$
$$K_2^{(1)} = \frac{b_1^{(1)}C_2^{(1)} + b_3^{(1)}C_4^{(1)}}{a_2^{(1)} + a_1^{(1)}}, \quad c_3^{(1)} = 0$$
$$c_4^{(1)} = \frac{1}{\lambda^{(1)}\gamma^{(1)} - (\zeta^{(1)})^2}(K_2^{(1)}(\gamma^{(1)} - \zeta^{(1)}) + K_2^{(1)}(\nu^{(1)}\gamma^{(1)} - \beta^{(1)}\zeta^{(1)}) - bC_2^{(1)}(X^{(1)}\zeta^{(1)} - Y^{(1)}\gamma^{(1)}) - bC_4^{(1)}(V^{(1)}\zeta^{(1)} - W^{(1)}\gamma^{(1)}))$$
$$l_3^{(1)} = 0, \quad l_4^{(1)} = \frac{1}{\gamma^{(1)}}(K_2^{(1)}(1+\beta^{(1)}) - c_4^{(1)}\zeta^{(1)} + bX^{(1)}C_2^{(1)} + bV^{(1)}C_4^{(1)}) \tag{17}$$

From Eq. (17), we find out that the temperature and moisture concentration remain constant within the solid cylinder; the constant values are the temperature and moisture concentration on the outer surface of the solid cylinder.

3.2 Multilayered Cylinder. We consider a hollow multilayered smart cylinder with inner radius a and outer radius b. To utilize the closed-form solutions obtained above for each homogenous cylindrical layer, the following new nondimensional parameters are defined:

$$\bar\sigma_{rr}^{(n)} = \frac{\sigma_{rr}^{(n)}}{c_{33}^{(1)}} = \frac{c_{33}^{(n)}}{c_{33}^{(1)}}\Sigma_{rr}^{(n)}; \quad \bar\sigma_{\theta\theta}^{(n)} = \frac{\sigma_{\theta\theta}^{(n)}}{c_{33}^{(1)}} = \frac{c_{33}^{(n)}}{c_{33}^{(1)}}\Sigma_{\theta\theta}^{(n)}$$
$$\bar\sigma_{zz}^{(n)} = \frac{\sigma_{zz}^{(n)}}{c_{33}^{(1)}} = \frac{c_{33}^{(n)}}{c_{33}^{(1)}}\Sigma_{zz}^{(n)}; \quad \bar U^{(n)} = \frac{u^{(n)}}{a}; \quad \rho = \frac{r}{a}$$
$$\bar\phi^{(n)} = \frac{e_{33}^{(1)}}{c_{33}^{(1)}}\frac{\phi^{(n)}}{a} = \frac{c_{33}^{(n)}}{c_{33}^{(1)}}\frac{e_{33}^{(1)}}{e_{33}^{(n)}}\Phi_1^{(n)}$$
$$\bar\varphi^{(n)} = \frac{d_{33}^{(1)}}{c_{33}^{(1)}}\frac{\varphi^{(n)}}{a} = \frac{c_{33}^{(n)}}{c_{33}^{(1)}}\frac{d_{33}^{(1)}}{d_{33}^{(n)}}\Psi_1^{(n)}; \quad \bar D_r^{(n)} = \frac{D_r^{(1)}}{e_{33}^{(1)}} = \frac{e_{33}^{(n)}}{e_{33}^{(1)}}D_{r1}^{(n)}$$
$$\bar B_r^{(n)} = \frac{B_r^{(n)}}{d_{33}^{(1)}} = \frac{d_{33}^{(n)}}{d_{33}^{(1)}}B_{r1}^{(n)}; \quad \bar\vartheta^{(n)} = \frac{\beta_1^{(1)}}{c_{33}^{(1)}}\vartheta^{(n)} = \frac{c_{33}^{(n)}}{c_{33}^{(1)}}\frac{\beta_1^{(1)}}{\beta_1^{(n)}}\Theta$$
$$\bar m^{(n)} = \frac{\xi_1^{(1)}}{c_{33}^{(1)}}m^{(n)} = \frac{c_{33}^{(n)}}{c_{33}^{(1)}}\frac{\xi_1^{(1)}}{\xi_1^{(n)}}M^{(n)}; \quad \Omega_{HTMEE} = \frac{\rho_d^{(1)}\omega^2 a^2}{c_{33}^{(1)}} \tag{18}$$

Note that by substituting a with b in Eq. (18), the new nondimensional parameters above could be used for a solid multilayered smart cylinder.

Since imperfectly bonded interfaces could have major effects on the reliability of designed composite structures, multiphysics imperfections of bonded interfaces are also considered. The imperfect interfaces investigated here are mechanically compliant with hygrothermomagnetoelectrically weak conduction. For highly conducting interfaces one can refer to Ref. [67]. The imperfect multiphysics interfacial conditions can be simulated by the generalized shear lag or spring layer model [68–70]. The following boundary and interfacial conditions are considered here for a hollow multilayered cylinder:

$$\bar\sigma_{rr}^{(1)}(\rho=1) = \bar\sigma_{rri}$$
$$\bar\sigma_{rr}^{(j)}(\rho=\rho_j) = \bar\sigma_{rr}^{(j+1)}(\rho=\rho_j)$$
$$\chi_u^{(j)}\bar\sigma_{rr}^{(j)}(\rho=\rho_j) = \bar U^{(j+1)}(\rho=\rho_j) - \bar U^{(j)}(\rho=\rho_j)\bar\sigma_{rr}^{(N)}(\rho=\rho_N) = \bar\sigma_{rro} \ (\chi_u^j \ge 0) \quad \text{(Elastic)} \tag{19a}$$

$$
\begin{aligned}
\bar{\phi}^{(1)}(\rho=1)&=\bar{\phi}_i\\
\bar{D}_r^{(j)}(\rho=\rho_j)&=\bar{D}_r^{(j+1)}(\rho=\rho_j)\\
\chi_\phi^{(j)}\bar{D}_r^{(j)}(\rho=\rho_j)&=\bar{\phi}^{(j+1)}(\rho=\rho_j)-\bar{\phi}^{(j)}(\rho=\rho_j)\bar{\phi}^{(N)}(\rho=\rho_N)\\
&=\bar{\phi}_o\ (\chi_\phi^j\le 0)\qquad \text{(Electric)}
\end{aligned}\tag{19b}
$$

$$
\begin{aligned}
\bar{\varphi}^{(1)}(\rho=1)&=\bar{\varphi}_i\\
\bar{B}_r^{(j)}(\rho=\rho_j)&=\bar{B}_r^{(j+1)}(\rho=\rho_j)\\
\chi_\phi^{(j)}\bar{B}_r^{(j)}(\rho=\rho_j)&=\bar{\varphi}^{(j+1)}(\rho=\rho_j)-\bar{\varphi}^{(j)}(\rho=\rho_j)\bar{\varphi}^{(N)}(\rho=\rho_N)\\
&=\bar{\varphi}_o\ (\chi_\varphi^j\le 0)\qquad \text{(Magnetic)}
\end{aligned}\tag{19c}
$$

$$
\begin{aligned}
\bar{\vartheta}^{(1)}(\rho=1)&=\bar{\vartheta}_i\\
q_r^{(j)}(\rho=\rho_j)&=q_r^{(j+1)}(\rho=\rho_j)\\
\chi_\theta^{(j)}q_r^{(j)}(\rho=\rho_j)&=\vartheta^{(j+1)}(\rho=\rho_j)-\vartheta^{(j)}(\rho=\rho_j)\bar{\vartheta}^{(N)}(\rho=\rho_N)\\
&=\bar{\vartheta}_o\ (\chi_\theta^j\le 0)\qquad \text{(Temperature)}
\end{aligned}\tag{19d}
$$

$$
\begin{aligned}
\bar{m}^{(1)}(\rho=1)&=\bar{m}_i\\
p_r^{(j)}(\rho=\rho_j)&=p_r^{(j+1)}(\rho=\rho_j)\\
\chi_m^{(i)}p_r^{(i)}(\rho=\rho_i)&=m^{(i+1)}(\rho=\rho_i)-m^{(i)}(\rho=\rho_i)\bar{m}^{(N)}(\rho=\rho_N)\\
&=\bar{m}_o\ (\chi_m^j\le 0)\ \ (j=1,2,\ldots,N-1)\ \text{(Moisture)}
\end{aligned}\tag{19e}
$$

where the aspect ratio is $\rho_N=b/a$; χ_u^j, χ_ϕ^j, χ_φ^j, χ_θ^j, and χ_m^j are, respectively, nondimensional elastic, electric, magnetic, thermal, and hygroscopic compliance constants of the imperfect interfaces. The perfectly bonded interfaces are also represented by $\chi_u^j=0$, $\chi_\phi^j=0$, $\chi_\varphi^j=0$, $\chi_\theta^j=0$, and $\chi_m^j=0$. For the case of hollow multilayered cylinder rested on Winkler-type elastic foundation on the inner or outer surfaces, the elastic boundary conditions (19*a*) are modified, respectively, by $\bar{\sigma}_{rr}^{(1)}(\rho=1)=K_{Wi}\bar{U}(\rho=1)$ or $\bar{\sigma}_{rr}^{(N)}(\rho=\rho_N)=-K_{Wo}\bar{U}(\rho=\rho_N)$, in which $K_W=k_w a/c_{33}^{(1)}$. Using Eqs. (12), (14), (18), and (19) results in a linear algebraic equation for integration constants

$$
[I_{MEE}]_{7N\times 7N}\{X_{MEE}\}_{7N\times 1}=\{J_{MEE}\}_{7N\times 1}\tag{20}
$$

in which $\{X_{MEE}\}$ is a $7N\times 1$ vector of integration constants $\{X_{MEE}\}^T=\{A^{(1)}C^{(1)}D^{(1)}E^{(1)}F^{(1)}G^{(1)}H^{(1)}\ldots A^{(N)}C^{(N)}D^{(N)}E^{(N)}F^{(N)}G^{(N)}H^{(N)}\}_{7N\times 1}$, $\{I_{MEE}\}$ is a $7N\times 7N$ matrix and $\{J_{MEE}\}$ is a $7N\times 1$ vector whose components are not given because of brevity. To solve the algebraic equation (20), the hygrothermal integration constants defined in Eq. (13) should be determined. The integration constants for temperature distribution in a hollow multilayered cylinder are obtained by using Eqs. (13*a*), (18), and (19*d*) and expressed by the algebraic equation

$$
[I_\theta]_{2N\times 2N}\{X_\theta\}_{2N\times 1}=\{J_\theta\}_{2N\times 1}\tag{21}
$$

Moreover, the integration constants for moisture concentration distribution are found similarly by using Eqs. (13*b*), (18), and (19*e*)

$$
[I_m]_{2N\times 2N}\{X_m\}_{2N\times 1}=\{J_m\}_{2N\times 1}\tag{22}
$$

where $\{X_\theta\}^T=\{C_1^{(1)}\ C_2^{(1)}\ \ldots\ C_1^{(N)}\ C_2^{(N)}\}$ and $\{X_m\}^T=\{C_3^{(1)}\ C_4^{(1)}\ \ldots\ C_3^{(N)}\ C_4^{(N)}\}$ are $2N\times 1$ vectors; $\{I_\theta\}$ and $\{I_m\}$ are $2N\times 2N$ matrices and $\{J_\theta\}$ and $\{J_m\}$ are $2N\times 1$ vectors whose components are not given because of brevity. Solving algebraic equations (21) and (22) provides the hygrothermal integration constants required to determine the multiphysics integration constants in Eq. (20).

A similar solution procedure is employed to analyze the multiphysics responses of a solid multilayered cylinder with imperfectly bonded interfaces and outer radius $R_N=b$. Using the modified nondimensional parameters of Eq. (18), by substituting a with b, and employing the following boundary and interfacial conditions, a closed-form solution is sought for the solid cylinder:

$$
\begin{aligned}
\bar{\sigma}_{rr}^{(j)}(\rho=\rho_j)&=\bar{\sigma}_{rr}^{(j+1)}(\rho=\rho_j)\\
\chi_u^{(j)}\bar{\sigma}_{rr}^{(j)}(\rho=\rho_j)&=\bar{U}^{(j+1)}(\rho=\rho_j)-\bar{U}^{(j)}(\rho=\rho_j)\\
\bar{\sigma}_{rr}^{(N)}(\rho=1)&=\bar{\sigma}_{rro}\ \ (\chi_u^j\ge 0)\qquad \text{(Elastic)}
\end{aligned}\tag{23a}
$$

$$
\begin{aligned}
\bar{D}_r^{(j)}(\rho=\rho_j)&=\bar{D}_r^{(j+1)}(\rho=\rho_j)\\
\chi_\phi^{(j)}\bar{D}_r^{(j)}(\rho=\rho_j)&=\bar{\phi}^{(j+1)}(\rho=\rho_j)-\bar{\phi}^{(j)}(\rho=\rho_j)\\
\bar{\phi}^{(N)}(\rho=1)&=\bar{\phi}_o\quad (\chi_\varphi^j\le 0)\qquad \text{(Electric)}
\end{aligned}\tag{23b}
$$

$$
\begin{aligned}
\bar{B}_r^{(j)}(\rho=\rho_j)&=\bar{B}_r^{(j+1)}(\rho=\rho_j)\\
\chi_\phi^{(j)}\bar{B}_r^{(j)}(\rho=\rho_j)&=\bar{\varphi}^{(j+1)}(\rho=\rho_j)-\bar{\varphi}^{(j)}(\rho=\rho_j)\\
\bar{\varphi}^{(N)}(\rho=1)&=\bar{\varphi}_o\quad (\chi_\varphi^j\le 0)\qquad \text{(Magnetic)}
\end{aligned}\tag{23c}
$$

$$
\begin{aligned}
q_r^{(j)}(\rho=\rho_j)&=q_r^{(j+1)}(\rho=\rho_j)\\
\chi_\theta^{(j)}q_r^{(j)}(\rho=\rho_j)&=\vartheta^{(j+1)}(\rho=\rho_j)-\vartheta^{(j)}(\rho=\rho_j)\\
\bar{\vartheta}^{(N)}(\rho=1)&=\bar{\vartheta}_o\quad (\chi_\theta^j\le 0)\qquad \text{(Temperature)}
\end{aligned}\tag{23d}
$$

$$
\begin{aligned}
p_r^{(j)}(\rho=\rho_j)&=p_r^{(j+1)}(\rho=\rho_j)\\
\chi_m^{(i)}p_r^{(i)}(\rho=\rho_i)&=m^{(i+1)}(\rho=\rho_i)-m^{(i)}(\rho=\rho_i)\\
\bar{m}^{(N)}(\rho=1)&=\bar{m}_o\ \ (\chi_m^j\le 0)\ \ (j=1,2,\ldots,N-1)\quad \text{(Moisture)}
\end{aligned}\tag{23e}
$$

where $\rho=r/b$. It is worth to note that similar to the hollow cylinder, the elastic boundary condition on the outer surface of the cylinder is modified for the solid multilayered cylinder rested on Winkler-type elastic foundation by $\bar{\sigma}_{rr}^{(N)}(\rho=1)=-K_{Wo}\bar{U}(\rho=1)$, in which $K_W=k_w b/c_{33}^{(1)}$. The multiphysics solutions (12) and (14) are employed for *N-1* hollow cylindrical layers and multiphysics solutions (16) are utilized for the internal cylindrical core. Using Eqs. (18) and (23) results in

$$
\begin{aligned}
&[I_{MEE}]_{(7(N-1)+3)\times(7(N-1)+3)}\{X_{MEE}\}_{(7(N-1)+3)\times 1}\\
&=\{J_{MEE}\}_{(7(N-1)+3)\times 1}
\end{aligned}\tag{24}
$$

in which $\{X_{MEE}\}$ is a $(7(N-1)+3)\times 1$ vector of integration constants $\{X_{MEE}\}^T=\{D^{(1)}\ F^{(1)}\ H^{(1)}\ A^{(2)}\ C^{(2)}\ D^{(2)}\ E^{(2)}\ F^{(2)}\ G^{(2)}\ H^{(2)}\ \ldots\ A^{(N)}\ C^{(N)}\ D^{(N)}\ E^{(N)}\ F^{(N)}\ G^{(N)}\ H^{(N)}\}$ and $\{I_{MEE}\}$ is a $(7(N-1)+3)\times(7(N-1)+3)$ matrix and $\{J_{MEE}\}$ is a $(7(N-1)+3)\times 1$ vector. As mentioned earlier, the steady-state temperature and moisture concentration throughout the solid multilayered cylinder are also the temperature and moisture concentration on the outer surface of the solid cylinder.

3.3 Functionally Graded Cylinder. Used for the analysis of FG cylinders, the solutions above enable removal of the stress discontinuity across the interfaces of a multilayered cylinder, thereby allowing a variation of material properties on the cylinder surfaces [71].

As described in Refs. [46,72] to simplify the mathematical complexity of considering arbitrary profiles of material properties, the FG cylinder could be modeled as a multilayered composite by conveniently dividing it into a number of homogenous layers. To replicate the smooth variation of material properties in an FGM, the material properties of each layer are assumed to approximate those of the FGM in that specific location. Increasing the number of artificial homogenous layers reduces the level of approximation. In this paper, the material properties of FG cylinders are assumed to vary according to the following power-law models for hollow and solid cylinders, respectively,

$$P(\rho) = P_i + (P_o - P_i)\left(\frac{\rho - 1}{\rho_N - 1}\right)^{n_P} \left(\text{Hollow cylinder: } \rho = \frac{r}{a}\right) \tag{25a}$$

$$P(\rho) = P_i + (P_o - P_i)\rho^{n_P} \left(\text{Solid cylinder: } \rho = \frac{r}{b}\right) \tag{25b}$$

in which P is any property of the FG cylinder and subscripts "i" and "o" denote the value of the property at the inner and outer surfaces, respectively; n_P also stands for the nonhomogeneity index of the corresponding material property P. For a solid multilayered cylinder, P_1 represents the material property on the axis. Moreover, it is noteworthy to mention that the closed-form expressions obtained in this paper for heterogeneous media are exact solutions to the governing equations of their multiphysics behavior. As such, they can be used in place of numerical finite element software, such as ANSYS, ABAQUS, and COMSOL Multiphysics.

4 Results

The results provided in this section for multilayered and FGM cylinders are verified with those in literature [5,73] obtained for homogenous composites. To this end, we consider the material properties (Table 2) of adaptive wood (AW) constructed of $BaTiO_3/CoFe_2O_4$ as well as MEE constructed of $BaTiO_3/CoFe_2O_4$ with 20% of volume fraction V_f. The other material properties are assumed to be: $k^T(\text{N/sK}) = 0.383$, $k^M(\text{m}^2/\text{s}) = 1731 \times 10^{-12}$, and $\rho_d(\text{kg/m}^3) = 660.8$. Without loss of generality, we assume the multiphysics imperfection constants for compliance do not change among interfaces; in addition, radial heat and moisture fluxes are, respectively, represented by the nondimensional terms: $\bar{q}_r^{(n)} = (a\beta_1^{(1)}/k^{T(1)}c_{33}^{(1)})q_r^{(n)}$ and $\bar{p}_r^{(n)} = (a\zeta_1^{(1)}/k^{M(1)}c_{33}^{(1)})p_r^{(1)}$.

4.1 Influence of Imperfect Multiphysics Interfaces.

Figure 2 illustrates the influence of imperfectly bonded interfaces on the structural responses of a hollow, multilayered, rotating, infinitely long, hygrothermomagnetoelectroelastic (HTMEE) cylinder. The cylinder is composed of three layers of adaptive wood (AW) with the prescribed material properties. The absolute values of nondimensional compliance constants for imperfect multiphysics interfaces are also assumed: $\chi_u = |\chi_\phi| = |\chi_\varphi| = |\chi_\theta| = |\chi_m| = \chi_{HTMEE}$. As defined in Eq. (19), all the compliance constants are nonpositive except the elastic compliance constant χ_u, which is non-negative. The aspect ratio, inner radius, and nondimensional angular velocity of the HTMEE cylinder are $\rho_N = 4$ $(N=3)$, $a=1$, and $\Omega_{HTMEE} = 1$, respectively. The cylinder is subjected to internal pressure and electromagnetic excitation on the inner surface of the cylinder while the outer surface experiences the temperature and moisture concentration rises. The following multiphysics boundary conditions are assumed for the analysis:

$$\begin{aligned}&\bar{\sigma}_{rr}(1) = -1, \quad \bar{\phi}(1) = 1, \quad \bar{\varphi}(1) = 1, \quad \bar{\vartheta}(1) = 0, \quad \bar{m}(1) = 0\\ &\bar{\sigma}_{rr} = (\rho_N) = 0, \ \ \bar{\phi}(\rho_N) = 0, \ \ \bar{\varphi}(\rho_N) = 0, \ \ \bar{\vartheta}(\rho_N) = 5, \ \ \bar{m}(\rho_N) = 5\end{aligned} \tag{26}$$

Conditions (26) could simulate the structural behavior of a pressure vessel constructed of adaptive wood components working at different environmental conditions of temperature and moisture concentration and actuated with electromagnetic fields. Figures 2(*a*) through 2(*l*) depict, respectively, the effect of imperfection compliance constant χ_{HTMEE} on the multiphysics responses. For perfectly bonded interfaces, $\chi_{HTMEE} = 0$, and the numeric results reproduce those in Ref. [5] for a rotating homogenous MEE cylinder under hygrothermal loading.

As expected from Eq. (19), Fig. 2 shows that the radial displacement, electric potential, magnetic potential, temperature change, and moisture concentration are discontinuous at the interfaces. Due to the unconstraint interfacial conditions for hoop and axial stresses, the discontinuity could also be observed in the hoop and axial stress distributions. As seen in Fig. 2(*a*), a higher χ_{HTMEE} leads to lower radial displacement on the inner surface of the cylinder, and results in a larger radial displacement on the outer surface. Likewise, Figs. 2(*b*) and 2(*c*) show that an increase of χ_{HTMEE} enhance the electric potential and absolute value of the radial electric displacement throughout the cylinder. Furthermore, a higher χ_{HTMEE} amplifies the maximum magnetic potential and reduces the radial magnetic induction within the cylinder (Figs. 2(*d*) and 2(*e*)). Figure 2(*f*), on the other hand, shows a decrease in the radial stresses throughout the cylinder by increasing χ_{HTMEE}. The tensile hoop and axial stresses on the inner surface and the compressive hoop and axial stresses on the outer surface of the cylinder decrease with increasingly larger χ_{HTMEE}, as illustrated in Figs. 2(*g*) and 2(*h*). The variation of hoop and axial stresses should be accurately determined to prohibit the potential fracture in piezoelectric and piezomagnetic components [74]. It is noteworthy to remind that the steady-state temperature and moisture concentration behave similarly due to the resemblance between the equations of Fourier heat conduction and Fickian moisture diffusion. Accordingly, as depicted in Figs. 2(*i*) through 2(*l*), the distribution of dimensionless temperature and radial heat flux are those obtained for moisture concentration change and radial moisture flux.

While Fig. 2 shows the multiphysics responses of a hollow cylinder, Fig. 3 illustrates the effect of each physical loading on the radial stress distribution of the composite cylinder. Based on the coupled multiphysics analysis, each nondimensional physical loading of mechanical σ_{HTMEE}, electric ϕ_{HTMEE}, magnetic Ψ_{HTMEE}, thermal Θ_{HTMEE}, hygroscopic M_{HTMEE}, and rotary inertia Ω_{HTMEE} is applied separately to the cylindrical structure and the radial stress distribution is sought. As seen in Fig. 3, under HTMEE loading the rotary inertia and hygrothermal loading have more influence on the superimposed multiphysics response.

Table 2 Material properties of adaptive wood (AW) and MEE constructed of $BaTiO_3/CoFe_2O_4$ [5,23,57]

Material property	AW	MEE$(V_f)_{BaTiO_3} = 0.2$
c_{33} (N/m^2)	2.695×10^{11}	2.413×10^{11}
c_{11} (N/m^2)	2.86×10^{11}	2.540×10^{11}
c_{13} (N/m^2)	1.705×10^{11}	1.445×10^{11}
c_{12} (N/m^2)	1.73×10^{11}	1.445×10^{11}
e_{31} (C/m^2)	-4.4	-1.212
e_{33} (C/m^2)	18.6	3.412
d_{31} (N/Am)	580.3	4.172×10^2
d_{33} (N/Am)	699.7	5.162×10^2
$\in_{33}$ (C^2/Nm^2)	9.3×10^{-11}	2.622×10^{-9}
g_{33} (Ns^2/C^2)	3.0×10^{-12}	2.162×10^{-9}
μ_{33} (Ns^2/C^2)	1.57×10^{-4}	1.305×10^{-4}
β_1 $(\text{N/m}^2\text{K})$	6.105×10^6	5.926×10^6
β_1 $(\text{N/m}^2\text{K})$	6.295×10^6	5.6×10^6
ξ_1 (Nm/kg)	1.6×10^{-4}	0
ξ_3 (Nm/kg)	1.1×10^{-4}	0
γ_1 (C/Km^2)	-13.0×10^{-5}	0
χ_1 (Cm/kg)	0	0
τ_1 (N/AmK)	6.0×10^{-3}	0
υ_1 (Nm^2/Akg)	0	0
k^T (N/sK)	0.383	1.2
k^M (m^2/s)	1731×10^{-12}	1731×10^{-12}
ρ_d (kg/m^3)	660.8	1204

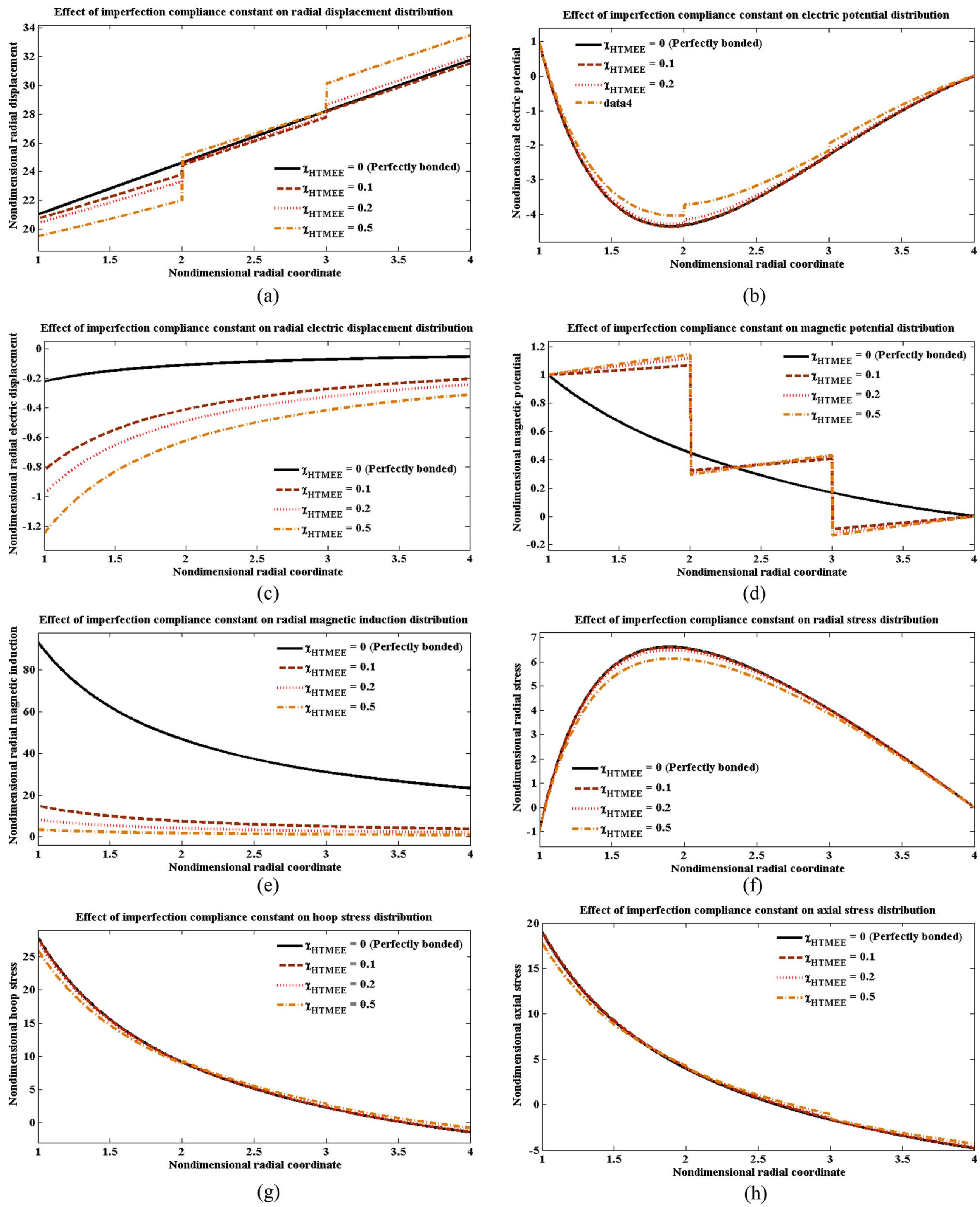

Fig. 2 Effect of imperfection compliance constants in a three-layer hollow cylinder

Figure 4 illustrates the multiphysics responses of an imperfectly bonded, solid, two-layer, infinitely long, rotating, HTMEE cylinder in the absence of hygrothermal loading. The solid cylinder is subjected to the following multiphysics excitation on its outer surface:

$$\bar{\sigma}_{rr}(1) = -1, \quad \bar{\phi}(1) = 1, \quad \bar{\varphi}(1) = 1, \quad \bar{\vartheta}(1) = 0, \quad \bar{m}(1) = 0 \tag{27}$$

The two-layer cylinder is constructed by bonding two AW layers. The outer radius and nondimensional angular velocity are,

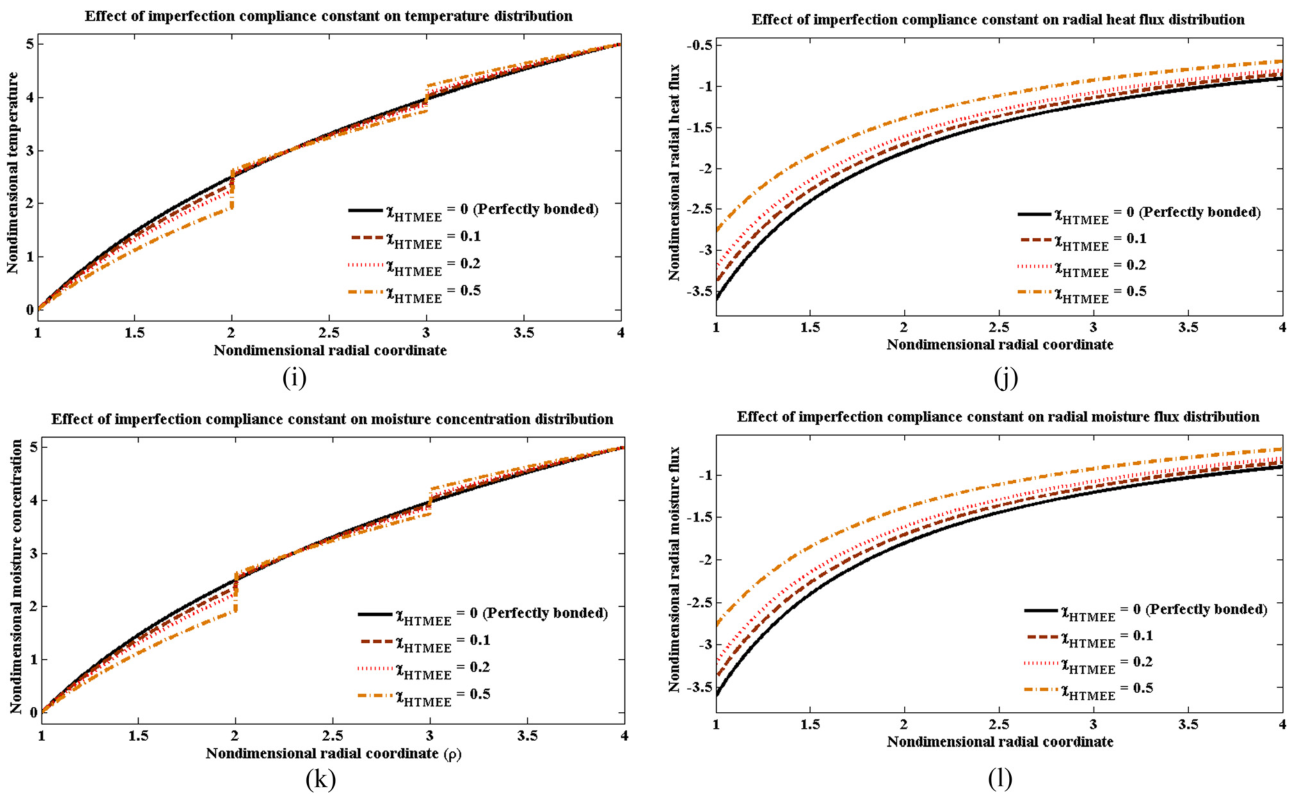

Fig. 2 (*Continued*)

respectively, assumed as $b = 1$ and $\Omega_{HTMEE} = 1$. Accordingly, the multiphysics boundary condition (27) represents a rotary composite shaft actuated with electromagnetic fields and working in a pressurized fluid with environmental temperature and moisture concentration. The influence of nondimensional compliance constants χ_{HTMEE} on the magnetoelectroelastic responses are depicted in Figs. 4(*a*) through 4(*d*). For a perfectly bonded solid cylinder, the multiphysics responses are aligned to those reported in Ref. [73]. Since the solid multiphysics cylinder posses zero radial electric displacement and radial magnetic potential according to the governing equation (5), the discontinuity is merely observed in the radial displacement, hoop stress, and axial stress distributions. As seen in Fig. 4(*a*), the absolute value of the radial displacement on the outer surface of the cylinder enhances by increasing the compliance constant. Furthermore, electric potential and magnetic potential on the axis of the solid cylinder decrease by amplifying the compliance constant, as seen in Figs. 4(*b*) and 4(*c*). The compressive radial stress within the solid cylinder decreases by increasing the compliance constant (Fig. 4(*d*)). It is worth mentioning that the value of radial displacement on the axis of the cylinder is finite; yet as explained in [5], the stress components could be singular on the axis depending on the material properties of HTMEE cylinder.

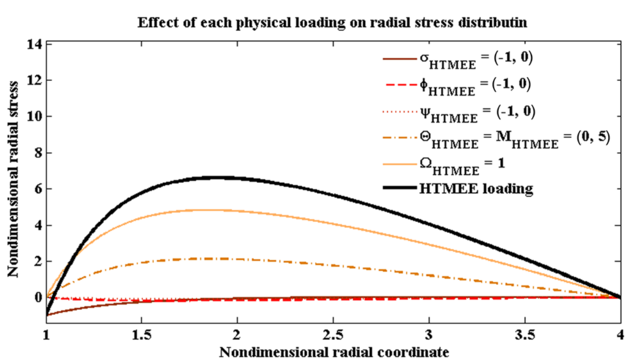

Fig. 3 Effect of each physical loading on the radial stress distribution

4.2 Influence of Electromagnetic Actuation. Figure 5 shows the effect of smart composite layers, used as an actuator, on the responses of a circular smart composite. For example, either an inner or outer layer of the multilayered composite could be actuated with an electromagnetic excitation applied on the inner or outer surface of a circular disk, while the other surface could be kept electromagnetically grounded. We consider an imperfectly bonded, hollow, three-layer, rotating HTMEE thin circular disk rested on Winkler-type elastic foundation on its inner surface with nondimensional foundation stiffness $K_W = 1$ subjected to different electromagnetic excitations. The multilayered HTMEE cylinder is assumed to be constructed of three homogenous AW layers. The aspect ratio, inner radius, nondimensional angular velocity, nondimensional imperfection compliance constant are, respectively, assumed $\rho_N = 4$ $(N = 3)$, $a = 1$, $\Omega_{HTMEE} = 1$, $\chi_{HTMEE} = 0.1$. The circular cylinder is subjected to pressure and temperature and moisture concentration rise on its outer surface as follows:

$$\bar{\vartheta}(1) = 0, \quad \bar{m}(1) = 0$$
$$\bar{\sigma}_{rr}(\rho_N) = -1, \quad \bar{\vartheta}(\rho_N) = 1, \quad \bar{m}(\rho_N) = 1 \tag{28}$$

These boundary conditions correspond to a rotary hollow composite disk rested on a flexible foundation, working in a pressurized hot fluid, and actuated with electromagnetic fields. The multilayered HTMEE circular disk experiences different nondimensional

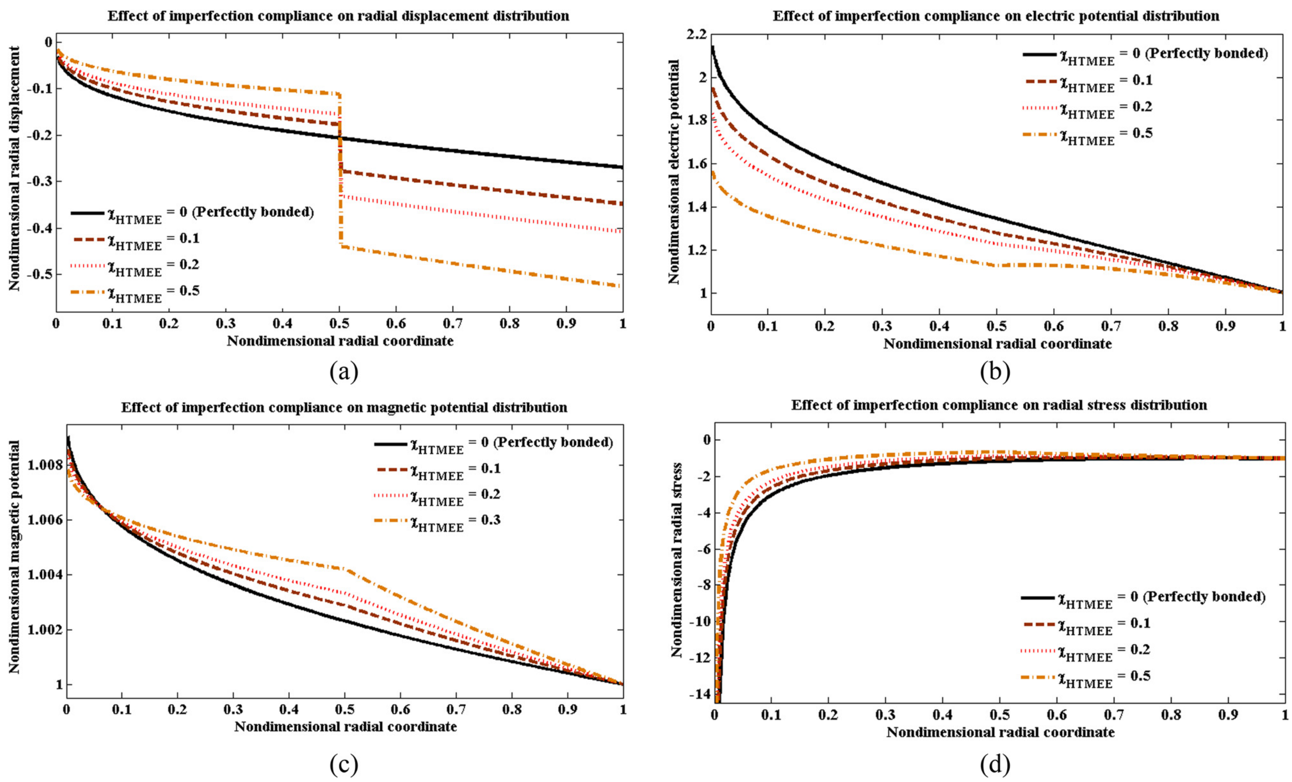

Fig. 4 Effect of imperfection compliance constants in a two-layer solid cylinder

electric potential ϕ_{HTMEE} and magnetic potential Ψ_{HTMEE} on its inner and outer surfaces.

The influence of increasing the electromagnetic excitation of actuator side on the structural responses of a three-layer smart circular disk is depicted in Fig. 5. The presence of an actuator on the inner and outer surface of the circular disk has opposite effect on the structural behavior of smart composite. It does not affect the temperature and moisture concentration change distribution due to the steady-state hygrothermomagnetoelectroelastic analysis. For the case of an inner actuator, Figs. 5(*a*), 5(*c*), and 5(*e*) show that greater electromagnetic excitations lead to lower radial displacement on the inner surface, higher radial displacement on the outer surface, and larger radial electric displacement and radial magnetic induction throughout the circular disk. Moreover, amplifying the value of electromagnetic excitation of the inner actuator reduces the radial stress throughout the circular disk, as illustrated in Fig. 5(*f*). The insight on the antagonist effects of the inner and outer actuation on the surface can be relevant to tailor the response of a smart cylinder to meet prescribed multiphysics requirements.

4.3 Influence of Heterogeneity. Figure 6 illustrates the influence of heterogeneity on the multiphysics responses of a perfectly bonded, hollow, three-layer, infinitely long HTMEE cylinder rested on Winkler-type elastic foundation on its outer surface. The three-layer HTMEE cylinder is constructed of two MEE layers with an embedded AW core (MEE/AW/MEE) and is subjected to the following multiphysics boundary conditions on its surfaces:

$$\begin{gathered}\bar{\sigma}_{rr}(1) = -1, \quad \bar{\phi}(1) = 1, \quad \bar{\varphi}(1) = 1, \quad \bar{\vartheta}(1) = 1, \quad \bar{m}(1) = 1 \\ \bar{\phi}(\rho_N) = 0, \quad \bar{\varphi}(\rho_N) = 0, \quad \bar{\vartheta}(\rho_N) = 0, \quad \bar{m}(\rho_N) = 0\end{gathered} \tag{29}$$

The aspect ratio, inner radius, nondimensional angular velocity, nondimensional imperfection compliance constant, and nondimensional foundation stiffness are specified as $\rho_N = 4$ ($N = 3$), $a = 1$, $\Omega_{HTMEE} = 0$, $\chi_{HTMEE} = 0$, and $K_W = 1$, respectively. The boundary condition (29) might simulate a composite pipe carrying a pressurized hot fluid located in soil and actuated by an electromagnetic field to control the structural responses. To investigate the effect of AW core on the structural responses of an MEE/AW/MEE multilayered cylinder, the behavior of the multilayered cylinder with different nondimensional AW thickness t_{AW} is compared with the behavior of a homogenous cylinder constructed of the MEE material.

Figure 6 shows that although multiphysics fields are continuous throughout the perfectly bonded nonhomogeneous multilayer composite, the hoop and axial stresses experience abrupt changes across the interfaces due to the difference between the material properties of the bonded layers. As shown in Fig. 6(*a*), increasing the thickness of the middle AW layer enhances the absolute value of the radial displacement on the inner surface of the cylinder. The effect of t_{AW} on the electric field is much more significant than on the magnetic field, as depicted in Figs. 6(*b*) and 6(*c*). The hoop stress also increases on the outer surface, as illustrated in Fig. 5(*f*). The insight on the antagonist effects of the inner and outer actuation on the surface can be relevant to tailor the response of a smart cylinder to meet prescribed multiphysics requirements. The greater t_{AW}, the higher the compressive radial stress throughout the cylinder, and the lower the compressive hoop and axial stresses on the inner surface of the cylinder. Changing the AW core thickness t_{AW} also alters the thermal responses of the structure but does not affect the hygroscopic field (Table 2).

4.3 Influence of Nonhomogeneity Indices. As revealed in Fig. 6, the presence of heterogeneity causes an abrupt change in the hoop and axial stresses across the interfaces of multilayered circular structures due to the different material properties of bonded layers. This phenomenon might result in debonding and crack initiation on the interfaces. As a result, FG smart structures

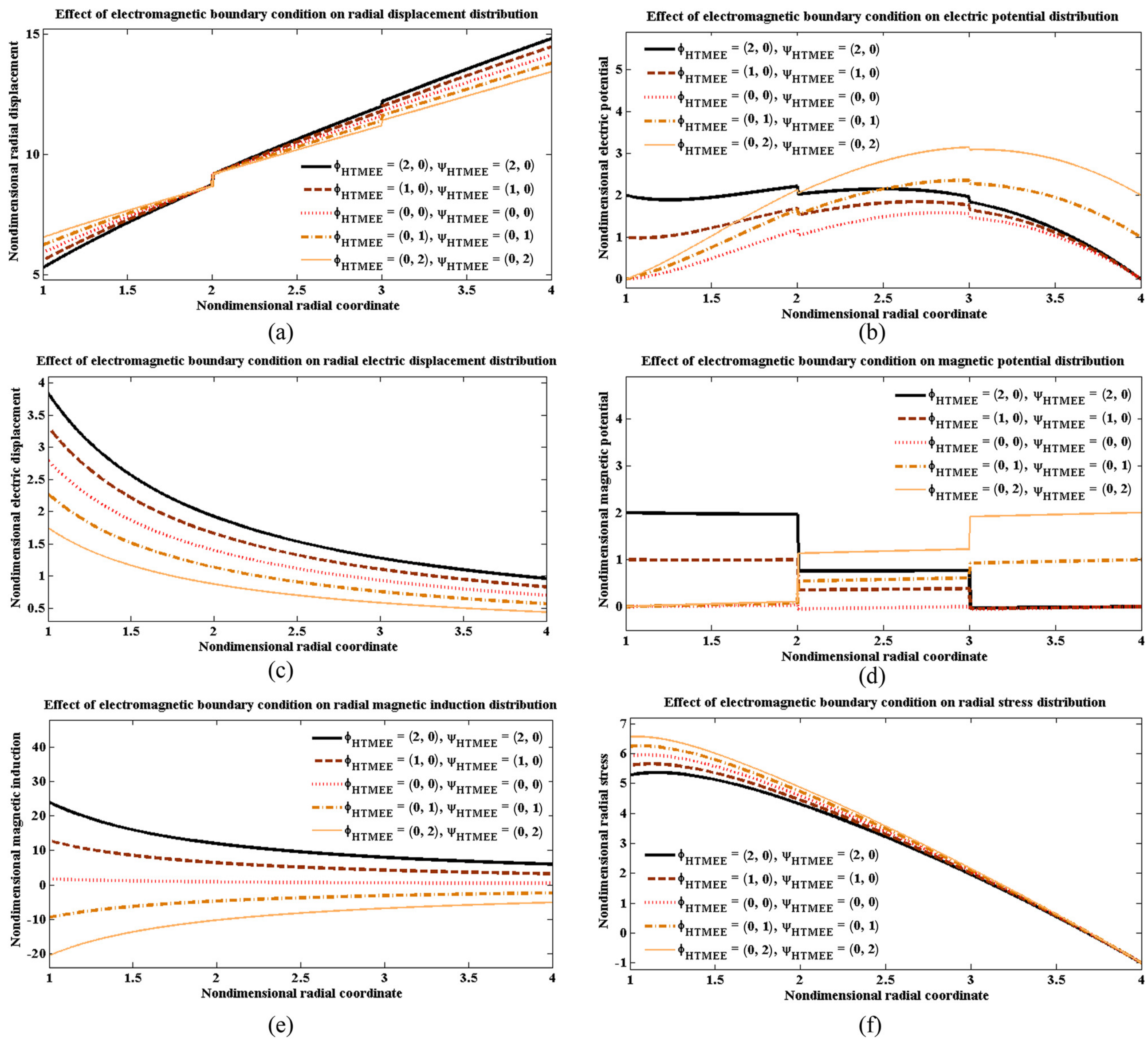

Fig. 5 Effect of electromagnetic boundary condition in a three-layer hollow circular disk

could be utilized to bypass the problem. Figure 7 presents the structural responses of rotating hollow FG HTMEE cylinder and thin circular disk rested on Winkler-type elastic foundation on its inner surface. The FG circular components are composed of MEE on the inner surfaces and AW on the outer surfaces and all material properties vary by a power-law formulation as specified in Eq. (25). To focus on the effect of nonhomogeneity indices on the multiphysics response, all nonhomogeneity indices are assumed to be equal $n_p = n$. The aspect ratio, inner radius, nondimensional angular velocity, and nondimensional foundation stiffness are respectively $\rho_N = 2$, $a = 1$, $\Omega_{HTMEE} = 1$, and $K_W = 1$. The multiphysics boundary conditions are also specified as follows:

$$\bar{\phi}(1) = 0, \quad \bar{\varphi}(1) = 0, \quad \bar{\vartheta}(1) = 0, \quad \bar{m}(1) = 0$$
$$\bar{\sigma}_{rr}(\rho_N) = -1, \quad \bar{\phi}(\rho_N) = 1, \quad \bar{\varphi}(\rho_N) = 1, \quad \bar{\vartheta}(\rho_N) = 1, \quad \bar{m}(\rho_N) = 1 \tag{30}$$

It is worthwhile noting that the FG media have been artificially divided to $N = 500$ layers to reproduce the FG profile. Moreover, the FG media could represent rotary circular components rested on a flexible foundation and subjected to a pressurized hot fluid, in which the outer surfaces of the composite have been electromagnetically actuated in order to control the structural responses.

As shown in Figs. 7(*a*) through 7(*f*), the multiphysics responses change continuously throughout the FG structure. The volume fraction of AW in the FG media enhances, if the nonhomogeneity indices increase, thereby leading to a decrease in the radial displacement of the inner surface and an increase in the radial displacement of the outer surface of FG circular thin disk, as shown in Fig. 7(*a*). Furthermore for FG circular disk, the electromagnetic field can also be tailored by varying the nonhomogeneity indices. As seen in Fig. 7(*b*), a high nonhomogeneity index results in lower electric potential. Also, magnetic potential does not reveal a strong dependency on the nonhomogeneity indices, as depicted in Fig. 7(*c*). Moreover, Fig. 7(*d*) shows that the tensile radial stress decreases by amplifying the nonhomogeneity indices. Although the aforementioned explanations relate to the multiphysics responses of FG circular thin disks, a similar trend could also be observed for FG hollow cylinders. As seen in Figs. 7(*a*), 7(*b*), and 7(*d*), radial displacement and radial stress for plane strain condition are higher than those for the plane stress condition; on the other hand, the electric potential is greater for plane stress condition. Nevertheless, plane strain and plane stress conditions do not

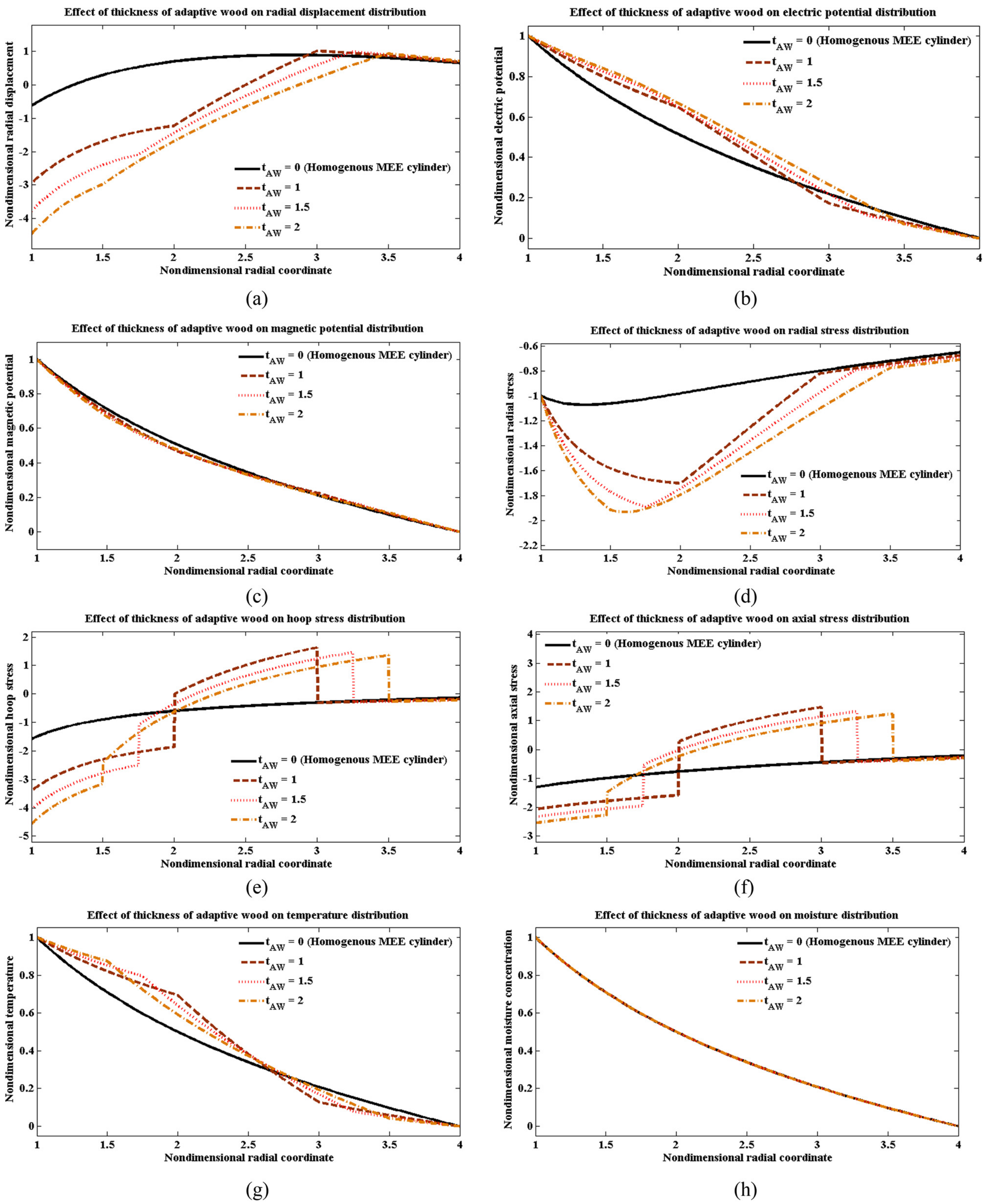

Fig. 6 Effect of thickness t_{AW} of adaptive wood in a three-layer composite cylinder

alter the uncoupled hygrothermal behavior. The temperature distribution changes by varying the nonhomogeneity indices; however, the hygroscopic responses are independent of the nonhomogeneity indices because of the prescribed hygroscopic material properties for MEE and AW (Figs. 7(*e*) and 7(*f*)). It should be mentioned that although prescribed nonhomogeneity indices were assigned for all material properties, the solution procedure developed in this paper can also be utilized to further investigate the effects of each nonhomogeneity index on the structural response and eventually optimize the response of an FG smart cylinder.

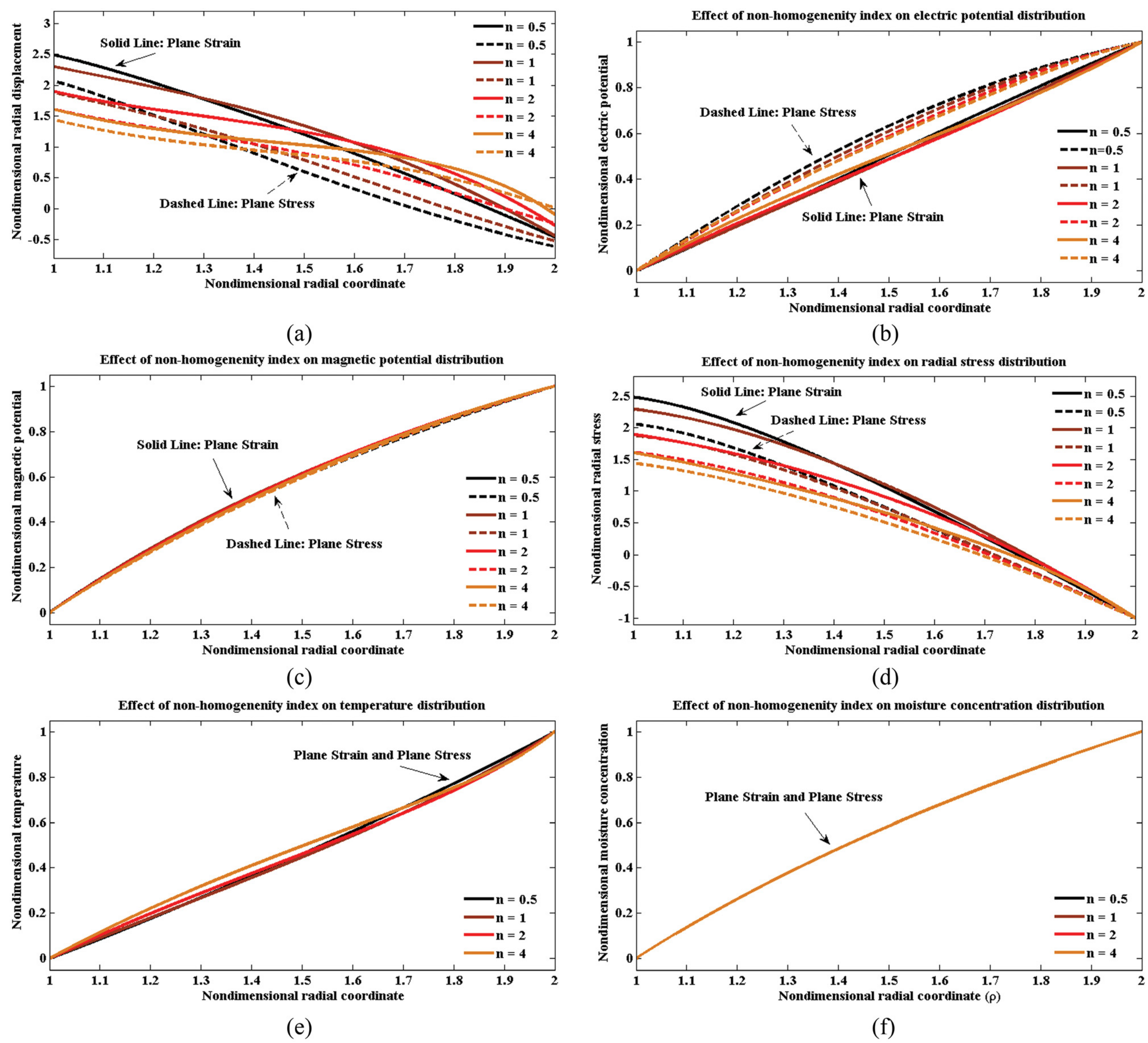

Fig. 7 Effect of nonhomogeneity index of FG hollow cylinder and circular disk

6 Conclusion

Closed-form solutions have been presented in this paper for steady-state multiphysics responses of multilayered and FG infinitely long cylinders and thin circular disks. Based on hygrothermomagnetoelectroelasticity theory, the effect of physical interactions among moisture, temperature, magnetic, electric, and elastic fields has been investigated on the structural behavior of cylindrical hollow and solid smart composites. The coupled governing differential equations have been first decoupled and solved in exact form for each multiphysics homogenous layer. Then boundary and perfectly/imperfectly bonded interfacial conditions have been imposed to solve the problem. The results allow investigation of the influence of bonding imperfections, heterogeneity of bonded layers, and nonhomogeneity indices of FG media.

The solutions obtained in this paper might be used as benchmark studies, including the verification of other analytic and numeric multiphysics problems. Moreover, the analysis could be used for fracture analysis and optimum design of multilayered smart composites. From this work we can draw the following points:

(1) Need to properly model the multiphysics imperfection. The radial displacement, electric potential, magnetic potential, temperature, and moisture concentration as well as hoop and axial stresses have revealed discontinuity at the interfaces of imperfectly bonded multilayered composite.
(2) Dependence of stress and electromagnetic field distributions on the imperfection compliance constants. The results show that in hollow cylindrical structures higher values of imperfection constants lead to lower radial electric displacements and magnetic inductions.
(3) Zero radial electric displacement, magnetic induction, heat flux, and moisture flux in solid smart cylinders. The discontinuous distributions of multiphysics fields are observed only in the radial displacement, as well as hoop and axial stresses.
(4) Similar behavior of steady-state temperature and moisture concentration due to the analogy of Fourier heat conduction and Fickian moisture diffusion equations. We have shown that, within hollow cylinders, an increase of the hygrothermal imperfection constant reduces the absolute value of heat and moisture fluxes.
(5) Structural geometry and electromagnetic excitation of actuators control the multiphysics response and inhibit failure initiation in smart laminates. For the case of actuator

placed on the inner surface, higher values of electromagnetic excitation lead to lower radial stresses throughout the structure, as well as lower and higher hoop stresses on the inner and outer surfaces of the smart cylinder, respectively.

(6) Smooth variation of multiphysics fields across the interfaces of an FGM improves the structural behavior of smart components. This insight suggests the potential to further optimize each nonhomogeneity index of an FGM cylinder.

References

[1] Krzhizhanovskaya, V., 2012, "Simulation of Multiphysics Multiscale Systems, 7th International Workshop," Procedia Computer Sci., **1**, pp. 603–605.

[2] Brown, D., and Messina, P., 2010, "Scientific Grand Challenges: Crosscutting Technologies for Computing at the Exascale," Office of Science, U.S. Department of Energy, February 2–4, Washington, DC.

[3] Altay, G., and Dokmeci, M. C., 2008, "Certain Hygrothermopiezoelectric Multi-Field Variational Principles for Smart Elastic Laminae," Mech. Adv. Mater. Struct., **15**, pp. 1–32.

[4] Smittakorn, W., and Heyliger, P. R., 2000, "A Discrete-Layer Model of Laminated Hygrothermopiezoelectric Plates," Mech. Compos. Mater. Struct., **7**, pp. 79–104.

[5] Akbarzadeh, A. H., and Chen, Z. T., 2012, "Magnetoelectroelastic Behavior of Rotating Cylinders Resting on an Elastic Foundation Under Hygrothermal Loading," Smart Mater. Struct., **21**, p. 125013.

[6] Huang, J. H., and Kuo, W. S., 1997, "The Analysis of Piezoelectric/Piezomagnetic Composite Materials Containing Ellipsoidal Inclusions," J. Appl. Phys., **81**(3), pp. 1378–1386.

[7] Li, J. Y., and Dunn, M. L., 1998, "Micromechanics of Magnetoelectroelastic Composite Materials: Average Fields and Effective Behavior," J. Intell. Mater. Syst. Struct., **9**, pp. 404–416.

[8] Raja, S., Sinha, P. K., Prathap, G., and Dwarakanathan, D., 2004, "Thermally Induced Vibration Control of Composite Plates and Shells With Piezoelectric Active Damping," Smart Mater. Struct., **13**, pp. 939–950.

[9] Georgiaes, A. V., Kalamkarov, A. L., and Challagulla, K. S., 2006, "Asymptotic Homogenization Model for Generally Orthotropic Reinforcing Networks in Smart Composite Plates," Smart Mater. Struct., **15**, pp. 1197–1210.

[10] Hassan, E. M., Kalamkarov, A. L., Georgiades, A. V., and Challagulla, K. S., 2009, "An Asymptotic Homogenization Model for Smart 3D Grid-Reinforced Composite Structures With Generally Orthotropic Constituents," Smart Mater. Struct., **18**, p. 075006.

[11] Zhang, P. W., Zhou, Z. G., and Wu, L. Z., 2009, "Coupled Field State Around Three Parallel Non-Symmetric Cracks in a Piezoelectric/Piezomagnetic Material Plane," Arch. Appl. Mech., **79**, pp. 965–979.

[12] Kundu, C. K., and Han, J. H., 2009, "Nonlinear Buckling Analysis of Hygrothermoelastic Composite Shell Panels Using Finite Element Method," Compos Part B, **40**, pp. 313–328.

[13] Chen, X., 2010, "Nonlinear Electro-Thermo-Viscoelasticity," Acta Mech., **211**, pp. 49–59.

[14] Mahato, P. K., and Maiti, D. K., 2010, "Flutter Control of Smart Composite Structures in Hygrothermal Environment," J. Aerosp. Eng., **23**, pp. 317–326.

[15] Babaei, M. H., and Akhras, G., 2011, "Temperature-Dependent Response of Radially Polarized Piezoceramic Cylinders to Harmonic Loadings," J. Intell. Mater. Syst. Struct., **22**, pp. 645–654.

[16] Akbarzadeh, A. H., Babaei, M. H., and Chen, 2011, "Coupled Thermopiezoelectric Behavior of a One-Dimensional Functionally Graded Piezoelectric Medium Based on C-T Theory," Proc. IMechE C: J. Mech. Eng. Sci., **225**, pp. 2537–2551.

[17] Kumar, R., Patil, H. S., and Lal, A., 2011, "Hygrothermoelastic Free Vibration Response of Laminated Composite Plates Resting on Elastic Foundations With Random System Properties: Micromechanical Model," J. Thermoplast. Compos. Mater., **26**(5), pp. 573–604.

[18] Wang, Q., and Yu, W., 2012, "Asymptotic Multiphysics Modeling of Composite Slender Structures," Smart Mater. Struct., **21**, p. 035002.

[19] Akbarzadeh, A. H., Abbasi, M., and Eslami, M. R., 2012, "Coupled Thermoelasticity of Functionally Graded Plates Based on Third-Order Shear Deformation Theory," Thin Walled Struct., **53**, pp. 141–155.

[20] Faruque Ali, S., and Adhikari, S., 2013, "Energy Harvesting Dynamic Vibration Absorbers," ASME J. Appl. Mech., **80**(4), p. 041004.

[21] Kondaiah, P., Shankar, K., and Ganesan, N., 2013, "Pyroelectric and Pyromagnetic Effects on Multiphase Magneto-Electro-Elastic Cylindrical Shells for Axisymmetric Temperature," Smart Mater. Struct., **22**, p. 025007.

[22] Balamurugani, V., and Narayanan, S., 2009, "Multilayer Higher Order Piezolaminated Smart Composite Shell Finite Element and Its Application to Active Vibration Control," J. Intell. Mater. Syst. Struct., **20**., pp. 425–441.

[23] Challagulla, K. S., and Georgiades, A. V., 2011, "Micromechanical Analysis of Magneto-Electro-Thermo-Elastic Composite Materials With Application to Multilayered Structures," Int. J. Eng. Sci., **49**, pp. 85–104.

[24] Xu, K., Noor, A. K., and Tang, Y. Y., 1995, "Three-Dimensional Solutions for Coupled Thermoelectroelastic Response of Multilayered Plates," Comput. Meth. Appl. Mech. Eng., **126**, pp. 355–371.

[25] Pan, E., 2001, "Exact Solution for Simply Supported and Multilayered Magneto-Electro-Elastic Plates," ASME J. Appl. Mech., **68**, pp. 608–618.

[26] Sayman, O., 2005, "Analysis of Multi-Layered Composite Cylinders Under Hygrothermal Loading," Compos. Part A, **36**, pp. 923–933.

[27] Shi, Z. F., Xiang, H. J., and Spencer, Jr., B. F., 2006, "Exact Analysis of Multi-Layer Piezoelectric/Composite Cantilevers," Smart Mater Struct **15**, pp. 1447–1458.

[28] Balamurugan, V., and Narayanan, S., 2007, "A Piezoelectric Higher-Order Plate Element for the Analysis of Multi-Layered Smart Composite Laminates," Smart Mater. Struct., **16**, pp. 2026–2039.

[29] Daga, A., Ganesan, N., and Shankar, K., 2008, "Transient Response of Magneto-Electro-Elastic Simply Supported Cylinder Using Finite Element," J. Mech. Mater. Struct., **3**(2), pp. 375–389.

[30] Wang, H. M., Liu, C. B., and Ding, H. J., 2009, "Dynamic Behavior of Piezoelectric/Magnetostrictive Composite Hollow Cylinder," Arch. Appl. Mech., **79**, pp. 753–771.

[31] Murin, J., and Kutis, V., 2009, "An Effective Multilayered Sandwich Beam-Link Finite Element for Solution of the Electro-Thermo-Structural Problems," Comput. Struct., **87**, pp. 1496–1507.

[32] Wang, R., Han, Q., and Pan, E., 2010, "An Analytical Solution for a Multilayered Magneto-Electro-Elastic Circular Plate Under Simply Lateral Boundary Condition," Smart Mater. Struct., **19**, p. 065025.

[33] Wan, Y. Yue, Y. and Zhong, Z., 2012, "Multilayered Piezomagnetic/Piezoelectric Composite With Periodic Interface Cracks Under Magnetic or Electric Field," Eng. Fract. Mech., **84**, pp. 132–145.

[34] Milazzo, A., and Orlando, C., 2012, "A Beam Finite Element for Magneto-Electro-Elastic Multilayered Composite Structures," Compos. Struct., **94**, pp. 3710–3721.

[35] Brischetto, S., 2013, "Hygrothermoelastic Analysis of Multilayered Composite and Sandwich Shells," J. Sandwich Struct. Mater., **15**(2), pp. 168–202.

[36] Fan, H., and Sze, K. Y., 2001, "A Micro-Mechanics Model for Imperfect Interface in Dielectric Materials," Mech. Mater., **33**, pp. 363–370.

[37] Bigoni, D., Serkov, S. K., Valentini, M., and Movchan, A. B., 1998, "Asymptotic Models of Dilute Composites With Imperfectly Bonded Inclusions," Int. J. Solids Struct., **35**(24), pp. 3239–3258.

[38] Icardi, U., 1999, "Free Vibration of Composite Beams Featuring Interlaminar Bonding Imperfections and Exposed to Thermomechanical Loading," Compos. Struct., **46**, pp. 229–243.

[39] Chen, W. Q., Cai, J. B., Ye, G. R., and Wang, Y. F., 2004, "Exact Three-Dimensional Solutions of Laminated Orthotropic Piezoelectric Rectangular Plates Featuring Interlaminar Bonding Imperfections Modeled by a General Spring Layer," Int. J. Solids Struct., **41**, pp. 5247–5263.

[40] Andrianov, I. V., Bolshakov, V. I., Danishevs'kyy, V. V., and Weichert, D., 2007, "Asymptotic Simulation of Imperfect Bonding in Periodic Fibre-Reinforced Composite Materials Under Axial Shear," Int. J. Mech. Sci., **49**, pp. 1344–1354.

[41] Mitra, M., and Gopalakrishnan, S., 2007, "Wave Propagation in Imperfectly Bonded Single Walled Carbon Nanotube-Polymer Composites," J. Appl. Phys., **102**, p. 084301.

[42] Wang, X., and Pan, E., 2007, "Magnetoelectric Effects in Multiferroic Fibrous Composite With imperfect Interface," Phys. Rev. B, **76**, pp. 214107.

[43] Melkumyan, A., and Mai, Y. W., 2008, "Influence of Imperfect Bonding on Interface Waves Guided by Piezoelectric/Piezomagnetic Composites," Phil. Mag., **88**(23), pp. 2965–2977.

[44] Wang, H. M., and Zou, L., 2013, "The Performance of a Piezoelectric Cantilevered Energy Harvester With an Imperfectly Bonded Interface," Smart Mater. Struct., **22**, p. 055018.

[45] Batra, R. C., 2008, "Optimal Design of Functionally Graded Incompressible Linear Elastic Cylinders and Spheres," AIAA J., **46**(8), pp. 2050–2057.

[46] Birman, V., and Byrd, L. W., 2007, "Modeling and Analysis of Functionally Graded Materials and Structures," ASME J. Appl. Mech., **60**, pp. 195–216.

[47] Pan, E., and Han, F., 2005, "Exact Solution for Functionally Graded and Layered Magneto-Electro-Elastic Plates," Int. J. Eng. Sci., **43**, pp. 321–339.

[48] Zhou, Z. G., Wu, L. Z., and Wang, B., 2005, "The Behavior of a Crack in Functionally Graded Piezoelectric/Piezomagnetic Materials Under Anti-Plane Shear Loading," Arch. Appl. Mech., **74**, pp. 526–535.

[49] Wang, H. M., and Ding, H. J., 2006, "Transient Responses of a Special Non-Homogeneous Magneto-Electro-Elastic Hollow Cylinder for a Fully Coupled Axisymmetric Plane Strain Problem," Acta Mech., **184**, pp. 137–157.

[50] Jiang, L. Y., 2008, "The Fracture Behavior of Functionally Graded Piezoelectric Materials With Dielectric Cracks," Int. J. Fract., **149**, pp. 87–104.

[51] Shen, H. S., 2009, "Nonlinear Bending of Functionally Graded Carbon Nanotube-Reinforced Composite Plates in Thermal Environments," Compos. Struct., **91**, pp. 9–19.

[52] Lee, J. M., and Ma, C. C., 2010, "Analytical Solutions for an Antiplane Problem of Two Dissimilar Functionally Graded Magnetoelectroelastic Half-Planes," Acta Mech., **212**, pp. 21–38.

[53] Akbarzadeh, A. H., Abbasi, M., Hosseini zad, S. K., and Eslami, M. R., 2011, "Dynamic Analysis of Functionally Graded Plates Using the Hybrid Fourier–Laplace Transform Under Thermomechanical Loading," Meccanica **46**, pp. 1373–1392.

[54] Kiani, Y., Akbarzadeh, A. H., Chen, Z. T., and Eslami, M. R., 2013, "Static and Dynamic Analysis of an FGM Doubly Curved Panel Resting on the Pasternak-Type Elastic Foundation," Compos. Struct., **94**, pp. 2474–2484.

[55] Panda, S., and Sopan G. G., 2013, "Nonlinear Analysis of Smart Functionally Graded Annular Sector Plates Using Cylindrically Orthotropic Piezoelectric Fiber Reinforced Composite," Int. J. Mech. Mater. Des., **9**, pp. 35–53.

[56] Kiani, Y., Sadighi, M., and Eslami, M. R., 2013, "Dynamic Analysis and Active Control of Smart Doubly Curved FGM Panels," Compos. Struct., **102**, pp. 205–216.

[57] Smittakorn, W., and Heyliger, P. R., 2001, "An Adaptive Wood Composite: Theory," Wood Fiber Sci., **33**(4), pp. 595–608.

[58] Youssef, H. M., 2005, "Generalized Thermoelasticity of an Infinite Body With a Cylindrical Cavity and Variable Material Properties". J. Therm. Stress., **28**, pp. 521–532.

[59] Hou, P. F., and Leung, A. Y. T., 2004, "The Transient Responses of Magneto-Electro-Elastic Hollow Cylinders," Smart Mater. Struct., **13**, pp. 762–776.

[60] Pan, E., and Heyliger, P. R., 2002, "Free Vibrations of Simply Supported and Multilayered Magneto-Electro-Elastic Plates," J. Sound Vib., **252**, pp. 429–442.

[61] Chen, P., and Shen, Y., 2007, "Propagation of Axial Shear Magneto–Electro-Elastic Waves in Piezoelectric–Piezomagnetic Composites With Randomly Distributed Cylindrical Inhomogeneities," Int. J. Solids Struct., **44**(5), pp. 1511–1532.

[62] Adelman, N. T., and Stavsky, Y., 1975, "Vibrations of Radially Polarized Composite Piezoeceramics Cylinders and Disks," J. Sound Vib., **43**(1), pp. 37–44.

[63] Adelman, N. T., Stavsky, Y., and Segal, E., "Axisymmetric Vibrations of Radially Polarized Piezoelectric Ceramic Cylinders," J. Sound Vib., **38**(2), pp. 245–254.

[64] Sih, G. C., Michopoulos, J. G., and Chou, S. C., 1986, *Hygrothermoelasticity*, Martinus Nijhoff Publishers, Dordrecht, Germany.

[65] Akbarzadeh, A. H., and Chen, Z. T., 2013, "Hygrothermal Stresses in One-Dimensional Functionally Graded Piezoelectric Media in Constant Magnetic Field," Compos. Struct., **97**, pp. 317–331.

[66] Akbarzadeh, A. H., and Chen, Z. T., 2012, "Thermo-Magneto-Electro-Elastic Responses of Rotating Hollow Cylinders," Mech. Adv. Mater. Struct., **21**(1), pp. 67–80.

[67] Chen, T., 2001, "Thermal Conduction of a Circular Inclusion With Variable Interface Parameter," Int. J. Solids Struct., **38**, pp. 3081–3097.

[68] Cheng, Z. Q., Jemah, A. K., and Williams, F. W., 1996, "Theory of Multilayered Anisotropic Plates With Weakened Interfaces," ASME J. Appl. Mech., **63**, pp. 1019–1026.

[69] Shodja, H. M., Tabatabaei, S. M., and Kamali, M. T., 2007, "A Piezoelectric Medium Containing a Cylindrical Inhomogeneity: Role of Electric Capacitors and Mechanical Imperfections," Int. J. Solids Struct., **44**, pp. 6361–6381.

[70] Wang, H. M., 2011, "Dynamic Electromechanical Behavior of a Triple-Layer Piezoelectric Composite Cylinder With Imperfect Interfaces," Appl. Math. Model., **35**(4), pp. 1765–1781.

[71] Jin, Z. H., and Batra, R. C., 1996, "Some Basic Fracture Mechanics Concepts in Functionally Graded Materials," J. Mech. Phys. Solids, **44**(8), pp. 1221–1235.

[72] Akbarzadeh, A. H. and Chen, Z. T., 2013, "Magnetoelastic Field of a Multilayered and Functionally Graded Cylinder With a Dynamic Polynomial Eigenstrain," ASME J. Appl. Mech., **81**(2), p. 021009.

[73] Babaei, M. H., and Chen, Z. T., 2008, "Exact Solutions for Radially Polarized and Magnetized Magnetoelectroelastic Rotating Cylinders," Smart Mater. Struct., **17**(2), p. 025035.

[74] Galic, D., and Horgan, C. O., 2003, "The Stress Response of Radially Polarized Rotating Piezoelectric Cylinders," ASME J. Appl. Mech., **70**, pp. 426–435.